Journal of Geophysical Research: Solid Earth

RESEARCH ARTICLE
10.1029/2017JB015124

# Observing and Modeling the Spectrum of a Slow Slip Event

**J. C. Hawthorne**[1] and **N. M. Bartlow**[2]

[1]Department of Earth Sciences, University of Oxford, Oxford, UK, [2]Department of Geological Sciences, University of Missouri, Columbia, MO, USA

**Key Points:**
- We estimate the moment rate power spectrum of slow slip events in Cascadia using GPS, strain, and tremor data
- We obtain a moment rate spectrum with shallow power law frequency decay at periods shorter than 1 day
- The spectrum can be reproduced if large slow slip events contain collections of subevents with linear moment-duration scaling

**Supporting Information:**
- Supporting Information S1

**Correspondence to:**
J. C. Hawthorne,
jessica.hawthorne@earth.ox.ac.uk

**Citation:**
Hawthorne J. C., & Bartlow, N. M. (2018). Observing and modeling the spectrum of a slow slip event. *Journal of Geophysical Research: Solid Earth*, *123*, 4243–4265. https://doi.org/10.1029/2017JB015124

Received 18 OCT 2017
Accepted 2 APR 2018
Accepted article online 6 APR 2018
Published online 8 MAY 2018

**Abstract** We estimate and model the normalized moment rate power spectrum of large slow slip events in Cascadia. We estimate the spectrum using data from GPS-derived slip inversions, borehole strain records, and beamforming-based tremor amplitudes. The normalized power spectrum initially decreases with frequency but then may flatten at periods of 1 to 10 days before decaying as frequency$^{-n_m}$ at higher frequencies, where $n_m$ is between 1.1 and 1.4 when estimated from tremor and between 0.4 and 1.5 when estimated from strain. We explore one way to understand the observed spectrum: by modeling a month-long slow slip event as the sum of a steady background moment rate and a population of subevents. The subevents represent the wide variety of observed slow earthquakes, ranging from 0.5-s-long tremor to 3-hr-long rapid tremor reversals. We parameterize the subevents' magnitude distribution and moment-duration scaling, and we examine how the subevent population determines the slow slip spectrum. There are not enough data to rigorously test the subevent model, but we show that the data are consistent with a single continuum of slow earthquakes whose moments scale linearly with their duration, as has been proposed previously.

## 1. Introduction

### 1.1. Bursts of Slip at a Range of Timescales

Large slow slip events contain numerous bursts of slip. The bursts are observed geodetically and via tremor, as day-long increases in migration rate (e.g., Kao et al., 2007; Ueno et al., 2010; Bartlow et al., 2011; Dragert & Wang, 2011; Bletery et al., 2017), several-hour-long rapid tremor reversals (RTRs; e.g., Obara, 2010; Ide, 2010a; Houston et al., 2011; Royer et al., 2015), 10-min- to hour-long tremor streaks and rapid tremor migrations (RTMs; e.g., Ghosh et al., 2010; Ryberg et al., 2010; Shelly, 2010; Rubin & Armbruster, 2013; Frank et al., 2014; Peng et al., 2015; Sun et al., 2015), 10 to 200-s-long $M_W$ 3–4 very low frequency earthquakes (VLFEs; Ito et al., 2007; Ide et al., 2008; Asano et al., 2015; Ghosh et al., 2015), and 0.2 to 0.7-s-long low-frequency earthquakes (LFEs), which constitute tremor (Obara, 2002; Shelly et al., 2007; Bostock et al., 2015; Thomas et al., 2016).

A variety of physical models have been proposed to explain all these bursts of increased moment rate. Bursts of rapid slip could represent ruptures of asperities or groups of asperities that have more unstable frictional properties than the rest of the plate interface (e.g., Ando et al., 2010; Nakata et al., 2011; Ando et al., 2012; Ghosh et al., 2012; Wallace et al., 2012; Yabe & Ide, 2014; Luo & Ampuero, 2017). For some friction laws, subevent ruptures can arise even without asperities, as the result of a complex evolving stress distribution (Rubin, 2011; Colella et al., 2012; Hawthorne & Rubin, 2013a). Complex stresses or material properties could also cause transient increases in the slipping area, with or without variations in slip rate (Ide, 2008, 2010b).

### 1.2. A Single Slow Earthquake Family, With One Moment-Duration Scaling?

Ide et al. (2007) proposed that all these bursts of slip, from LFEs to RTRs to large slow slip events, are components of a single slow earthquake family. Most well-observed slow earthquakes have roughly the same moment to duration ratio, or average moment rate (e.g., Ide et al., 2007; Heki & Kataoka, 2008; Ide et al., 2008; Aguiar et al., 2009; Matsuzawa et al., 2009; Wallace & Beavan, 2010; Gao et al., 2012; Fu & Freymueller, 2013; Rubin & Armbruster, 2013; Tsang et al., 2015; Hawthorne et al., 2016). The proposed magnitude-independent moment rate is intriguing, because it would imply that smaller slow earthquakes, with smaller areas, have higher average slip rates. Slip rates increase from <0.1 μm/s in large slow slip events to of order 1 mm/s in tremor (e.g., Dragert et al., 2001; Wallace et al., 2012; Bostock et al., 2015). If there is truly just one family of slow earthquakes, this large range of slip rates would likely have to be produced by a single deformation mechanism.

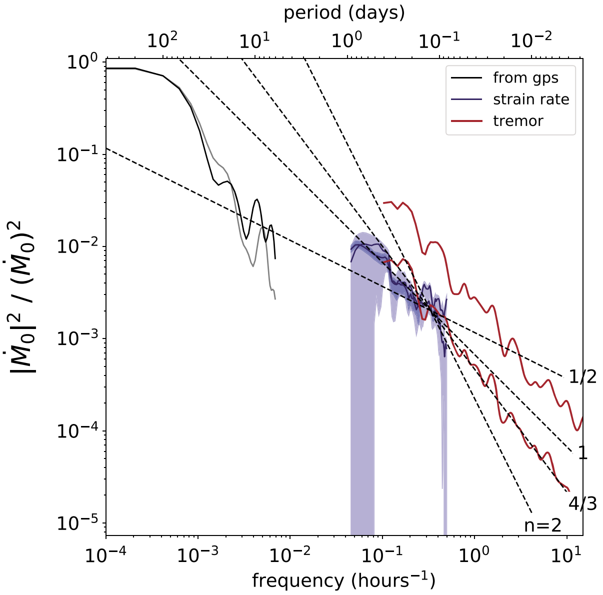

**Figure 1.** Moment rate power spectra inferred from the data, from (black and gray) the GPS-based slip inversions of Bartlow et al. (2011) and Wech and Bartlow (2014), (blue) the normalized strain rate data from stations B003 and B004, and (red) the beamforming-based tremor amplitude (lower) and amplitude squared (upper), from Ghosh et al. (2009). Shading around the strain estimates indicates the 70% confidence ranges. Dashed lines mark scalings as frequency$^{-n_m}$, with $n_m$ as labeled.

On the other hand, it is also possible that the apparently linear moment-duration scaling results at least in part from observational bias (Peng & Gomberg, 2010; Gomberg, Wech et al., 2016). The slow earthquake family could lack a systematic scaling (Peng & Gomberg, 2010), or there might be two slow earthquake families: slow slip and tremor. An important potential break in the scaling may be indicated by the small number of $M_W$ 3.5–5.5 slow earthquakes observed at subduction zones. This apparent gap in the slow earthquake population could reflect the noise level (Peng & Gomberg, 2010; Ide, 2014), but it could also divide slow slip and tremor. The gap may indicate that slow slip and tremor are governed by different physical processes. Slip rates in slow slip events are low and likely limited by the rheology of the plate interface (e.g., Liu & Rice, 2005, 2007; Shibazaki & Shimamoto, 2007; Segall et al., 2010; Hawthorne & Rubin, 2013b). Slip rates in tremor and VLFEs are higher and may be limited by seismic wave generation (e.g., Rice, 1993; Rubin & Ampuero, 2005).

If there is just one physical mechanism governing slow slip, tremor, and all the slow earthquakes in between, one might expect a power law, or fractal, distribution of slow earthquake sizes. Wech et al. (2010) identified a power law distribution of durations for small slow slip events in Cascadia. A power law distribution is also an acceptable match to the number of tremor migrations with various durations, as identified by Obara (2012) beneath the Kii Peninsula and by Bletery et al. (2017) in Cascadia. On the other hand, detections of LFEs in tremor appear to indicate a characteristic LFE size, with a restricted magnitude range. LFE moment distributions are best fit with *b* values greater than 4 or 5 or exponential distributions (Watanabe et al., 2007; Shelly & Hardebeck, 2010; Chamberlain et al., 2014; Sweet et al., 2014; Bostock et al., 2015; Chestler & Creager, 2017a).

### 1.3. Summary of Our Analysis

In this paper, we further assess the plausibility of a single slow earthquake family by examining the power that slow earthquakes could generate at a wide range of periods. We estimate and then attempt to model the moment rate power spectrum of large slow slip events in Cascadia.

To begin, we focus exclusively on the data. In sections 2–4, we use Global Positioning System-, strain-, and tremor-derived data to estimate the power in the slow slip moment rate at periods between 4 min and 200 days. We examine data from several slow slip events and plot them together in a normalized moment rate power spectrum, shown in Figure 1. Our analysis suggests that the moment rate power (1) initially decreases with increasing frequency but then (2) is unconstrained but potentially flat at frequencies of 0.1 to 1 day$^{-1}$, before (3) decreasing as frequency$^{-n_m}$ at higher frequencies, where $n_m$ is between 0.4 and 1.5.

In section 5, we examine how subevents could contribute to the moment rate power at various frequencies.We construct synthetic large slow slip events as the sum of a steady background moment rate and a population of subevents with a range of moments and durations. We find that the modeled spectra have shapes similar to the data-derived spectrum, and we develop a quantitative understanding of how the spectrum depends on the subevent population.

Finally, in sections 6 and 7, we compare the model with the observations. There are not currently enough data to rigorously test the model, but we show that the data and model are consistent with the linear moment-duration scaling that has been proposed to describe a single slow earthquake family (e.g., Ide et al., 2007; Gao et al., 2012; Ide, 2014).

## 2. Spectra From GPS-Derived Moment Rates

We estimate the slow slip moment rate (power) spectrum at periods longer than 6 days from two GPS-based slip inversions: one performed by Bartlow et al. (2011) for the August 2009 $M_W$ 6.8 slow slip event in Washington and Oregon and one performed by Wech and Bartlow (2014) for the similarly located $M_W$ 6.9 slow slip event beginning in June 2011 (Figure 2). These studies estimated the slip rate on a mesh of triangular subfaults representing the plate interface for each day throughout the two slow slip events using the Network Inversion Filter method (NIF; Segall and Matthews (1997), Miyazaki et al. (2006).

The NIF inverts a network of GPS stations for a time-dependent model of slip and slip rate on a specified fault surface. Normalized moment (or potency) rate is calculated by multiplying either differential slip or slip rate by the area of each subfault and summing. Details are given in section S1 in the supporting information. The estimated moment rates and their spectra are shown in Figure 3.

The power spectrum has value near $\bar{\dot{M}}_0^2$ at the lowest frequencies, where the period is longer than the slow slip interval. For these frequencies, all of the moment appears to accumulate during a small part of the cycle. When we compute the Fourier coefficient $\hat{\dot{M}}_0(f)$, defined in equation (S1) as $T_c^{-1} \int_0^{T_c} \dot{M}(t) e^{i2\pi ft} \mathrm{d}t$, where $T_c$ is a window longer than the slow slip event, we find that $|\hat{\dot{M}}_0(f)|$ tends to the time-averaged moment rate $\bar{\dot{M}}_0$. The power decreases at higher frequencies, as the period gets shorter than the slow slip duration, and moment is distributed over a large part of the cycle.

However, the rapid spectral falloff at very high frequencies, larger than 0.1 or 0.2 day$^{-1}$, is likely an artifact of smoothing in the slip inversion (see section S1). With the NIF inversion, it is not straightforward to calculate the frequency at which temporal smoothing becomes important. We choose to interpret the data only at periods longer than 6 days, because Bartlow et al. (2011) show that smoothing significantly affects the slip inversion at periods shorter than a few days (their Figure S2) and because the higher-frequency spectral decay is consistent with noise smoothed by the NIF (see section S1). At longer periods, the slip inversion appears to reproduce the amplitude of the well-resolved signal in the GPS data (Figure S1 of Bartlow et al. (2011)).

## 3. Spectra From Borehole Strain Observations

### 3.1. Data Selection and Processing

To analyze the slow slip moment rate spectrum at high frequencies, between 1 day$^{-1}$ and 1 hr$^{-1}$, we use borehole strain observations from two Plate Boundary Observatory strainmeters, B003 and B004, located in the northwestern Olympic Peninsula (Figure 2). These strainmeters have recorded eight well-resolved slow slip events, as seen in Figures 4 and S1 – S3 and previously analyzed by, for example, Dragert and Wang (2011), Roeloffs (2015), and Krogstad (2016).

We analyze just one of the three components of horizontal strain at each strainmeter, which we refer to as $\epsilon_{\text{LCV-na}}$, because this component of strain appears to have lower noise than the other two components. We isolate the component of interest in section S2 by first identifying two components with low sensitivity to atmospheric pressure variations (Wang et al., 2008; Roeloffs, 2010; Dragert & Wang, 2011; Hodgkinson et al., 2013; Hawthorne et al., 2016) and then using principal component analysis to isolate the lowest-noise component (e.g., Bishop, 2006; Press, 2007; Rangelova et al., 2007; Kositsky & Avouac, 2010; Ji & Herring, 2013).

Once we have selected the component to consider, we estimate and correct for two nontectonic signals: tidal and diurnal variations (Hart et al., 1996; Langbein, 2010; Roeloffs, 2010; Hodgkinson et al., 2013, following the procedure of Hawthorne et al., 2016). We use the 10-year-long corrected $\epsilon_{\text{LCV-na}}$ records for all of our analysis.

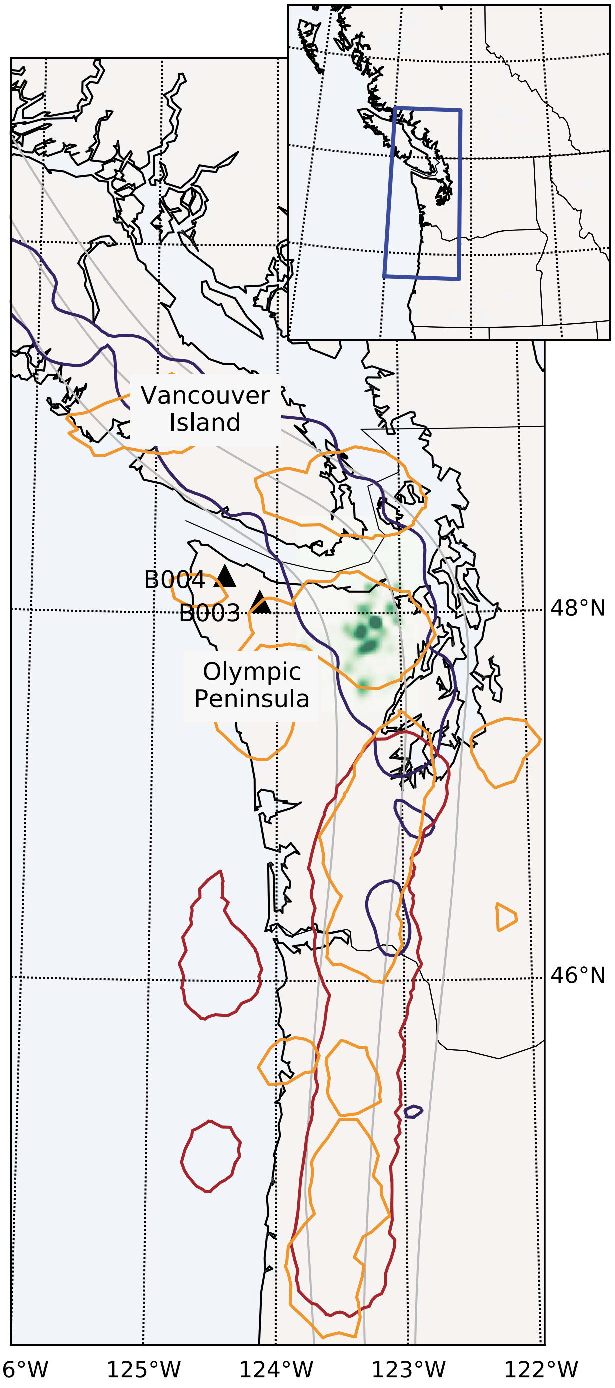

**Figure 2.** Locations of Plate Boundary Observatory strainmeters (black triangles) and the investigated tremor and slow slip events. Green shading near 48°N shows tremor locations identified by Ghosh et al. (2009). The blue curve illustrates slow slip locations relevant for the strain analysis. It outlines 95% of the tremor locations identified in large post-2009 slow slip events centered around northern Washington by Wech and Creager (2008). Red and orange curves indicate 1.5-cm contours of slip in the southern 2009 and 2011 slow slip events, as inferred from GPS data by Bartlow et al. (2011) and Wech and Bartlow (2014).

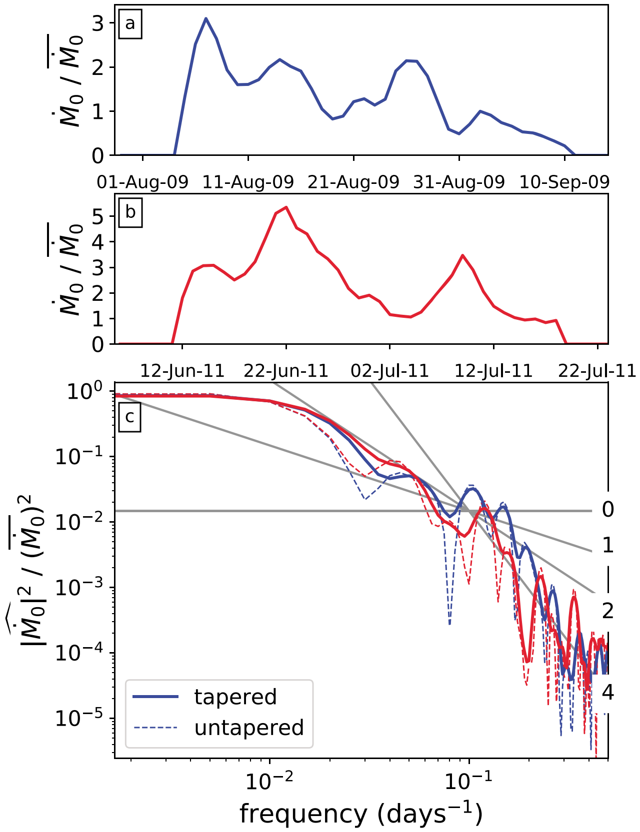

**Figure 3.** (a) Slow slip moment rate during the 2009 event, estimated from the Global Positioning System-based slip inversion of Bartlow et al. (2011) and normalized by the average moment rate in the slow slip interval. (b) Normalized slow slip moment rate during the 2011 event, estimated by Wech and Bartlow (2014). (c) Normalized moment rate power spectra of the 2009 (blue) and 2011 (red) events, computed with (solid) and without (dashed) a multitaper approach (e.g., Percival & Walden, 1993; Thomson, 1982). Gray lines indicate scalings as frequency$^{-n_m}$, where $n_m$ is as labeled.

### 3.2. Spectra for Several Slow Slip Intervals

We use the strain data to infer moment rate variations during 4- to 8-day-long portions of the slow slip events, marked in blue in Figure 4. We choose these intervals because strain accumulates roughly linearly with time during each one, so we may approximate that the location of slip changes only modestly. We assume that the Green's function is constant within each interval and that variations in strain rate $\dot{\epsilon}(t)$ result only from variations in the slow slip moment rate $\dot{M}_0$, so that $\dot{\epsilon}(t) = \text{constant} \times \dot{M}_0(t)$ (Hawthorne & Rubin, 2010; Hawthorne et al., 2016). We confirm that this linear $\dot{\epsilon}(t)$-$\dot{M}_0$ scaling is sufficiently accurate for our analysis in section S5, where we generate and analyze synthetic strain time series for slow slip events in Cascadia (Okada, 1985; Wech & Creager, 2008; McCrory et al., 2012).

With a linear scaling between $\dot{\epsilon}$ and $\dot{M}_0$, the strain rate power spectrum $|\hat{\dot{\epsilon}}(f)|^2$ should be equal to a constant multiplied by the moment rate power spectrum $|\hat{\dot{M}}_0(f)|^2$. However, the original data are the strain time series, so we begin by estimating the strain power spectrum $|\hat{\epsilon}(f)|^2$ in each slow slip interval. To prepare the data, we high-pass filter the 10-year record with a corner frequency of 0.5 day$^{-1}$, eliminating signals at periods longer than the intervals. Then we extract the strain data from each interval, detrend, and compute the spectra with a multitaper approach (e.g., Thomson, 1982; Percival & Walden, 1993). The resulting power spectra are shown in Figure 5. They have been normalized only by interval length, so that the *y* value indicates $|\hat{\epsilon}(f)|^2$, the squared (half) amplitude of the sinusoid observed at each frequency.

Also plotted in Figure 5 are spectra of representative noise intervals, taken from intervals 40 days before the relevant slow slip intervals. At periods between 4 hr and 3 days, the noise power spectra are mostly a factor of few smaller than the spectra observed during slow slip events. The noise spectra are variable, but many roughly follow a frequency$^{-2}$ decay (gray line) at periods between 2 and 12 hr, consistent with random walk noise that is commonly observed in strain records (e.g., Langbein, 2010, 2004; Hawthorne & Rubin, 2013c).

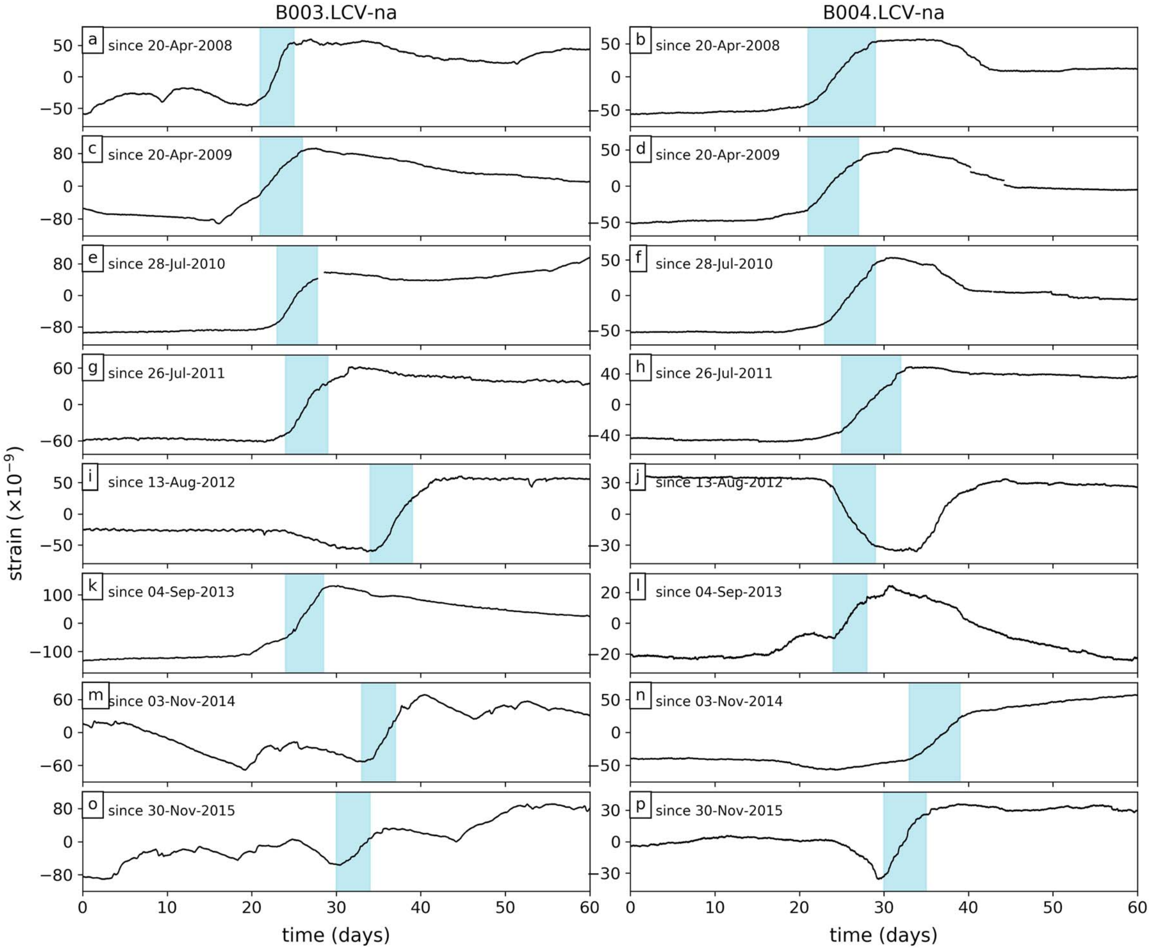

**Figure 4.** Corrected strain time series for $\varepsilon_{\text{LCV-na}}$ at B003 (column 1) and B004 (column 2) during various slow slip intervals. The dates in the upper left corners indicate time 0 in each of the plots. A linear trend estimated from days −15 to 10 in each plot has been removed. Blue bars mark the slow slip intervals used in our analysis.

The strain power spectra $|\hat{\varepsilon}(f)|^2$ in the slow slip intervals decrease roughly as frequency$^{-3}$ at frequencies between 0.05 and 0.5 hr$^{-1}$. A frequency$^{-3}$ decay in the strain power spectra implies a roughly frequency$^{-1}$ decay in the strain rate power spectra $|\hat{\dot{\varepsilon}}(f)|^2$—and by inference a roughly frequency$^{-1}$ decay in the moment rate power spectra $|\hat{\dot{M}}_0(f)|^2$.

### 3.3. Spectra Averaged Over Multiple Slow Slip Intervals

#### 3.3.1. Estimating the True Slow Slip Power: Observed Minus Noise

In order to more accurately estimate the strain spectra, we average power spectra from seven of the eight slow slip events observed at each station, obtaining the black lines in Figure 6. We exclude the 2013 slow slip event because its spectrum is exceptionally large (though including it does not change our conclusions; see section S4.1). The remaining spectra have similar amplitudes, and we average without weighting or normalization.

We also compute average power spectra for 18 sets of noise intervals. The noise interval times are defined by shifting the slow slip intervals forward or backward by 4 to 12 weeks. The median of the 18 estimates of noise power at each frequency are marked by the red line in Figure 6, and the central 70% of the noise estimates are shown by the pink shading.

The power contributed by the slow slip event can now be estimated as the power observed during slow slip (black lines) minus the power attributed to noise (red lines and shading). This difference is plotted in blue in Figure 6, but it is poorly resolved at high and low frequencies. At high frequencies (>1 hr$^{-1}$), the slow slip power cannot be differentiated from zero with 70% confidence. At very low frequencies (< 0.05 hr$^{-1}$),

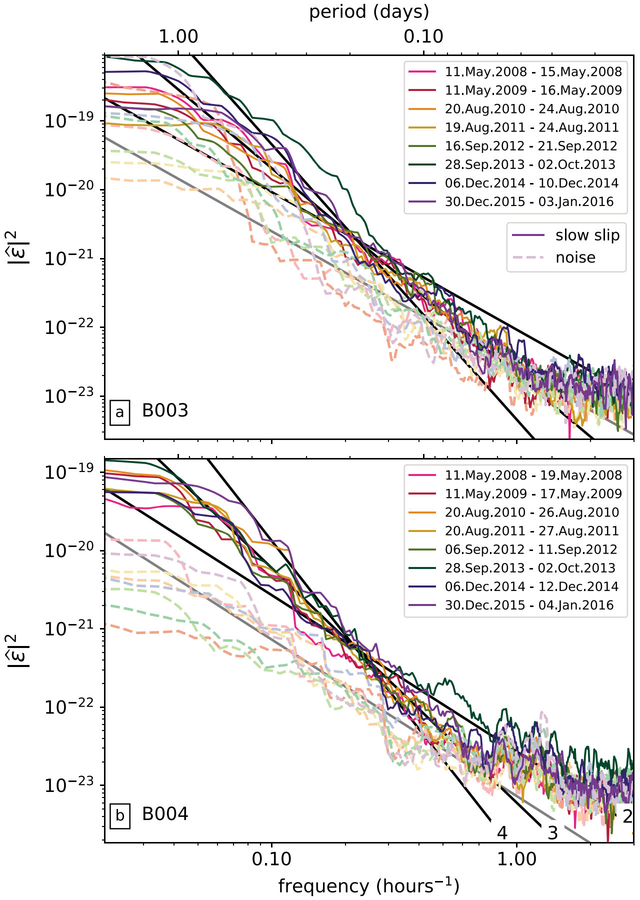

**Figure 5.** Solid colored curves: power spectra of strain observed at (a) B003 and (b) B004 during the slow slip intervals listed in the legend and marked in blue in Figure 4. Dashed pastel curves: power spectra of strain during noise intervals, taken 40 days before the slow slip interval shown in the same color. Diagonal black lines indicate scalings as frequency $f^{-2}$, $f^{-3}$, and $f^{-4}$, as labeled. The diagonal gray line indicates frequency $f^{-2}$ scaling.

the power cannot be interpreted because the spectra are influenced by the high-pass filtering and tapering described in section 3.2. At frequencies from 0.05 to 1 hr$^{-1}$, on the other hand, our estimates of the true slow slip strain power are well constrained and appear to decay roughly as frequency$^{-3}$ (central black dashed lines in Figure 6).

### 3.3.2. Fitting the Spectral Decay Rate

To better quantify the spectral decay rate, we model the 1 day$^{-1}$ to 0.7 hr$^{-1}$ portion of the strain spectra as a power law in frequency: as $a_r f^{-(2+n_s)}$, with frequency $f$ in days. We grid search over $a_r$ and $n_s$ and compute the probability that the spectrum predicted by each parameter pair matches the spectrum estimated from the data. Details are given in section S4.2, and parameter probabilities are shown in Figure S6. The estimated probability densities imply 90% confidence ranges on the strain rate decay exponent $n_s$ between 0.39 and 0.91 for B003 and between 0.73 and 1.48 for B004, with most likely exponents of 0.62 and 1.08, respectively.

In computing these confidence intervals, we have chosen the filtering frequencies and interval sizes that are most appropriate given the data and analysis approach. However, we also redo our frequency decay fits with a wider range of filtering and interval parameters in section S4.3. All of the 90% confidence intervals obtained imply a decay rate $n_s$ between 0.32 to 2.04.

### 3.3.3. Estimating Fractional Moment Rate Variations

The unnormalized spectra provide useful estimates of the spectral shape. But to estimate the overall amplitude—how much the moment varies around its mean, we must normalize the spectra. As noted in section 3.2, we have chosen intervals with roughly linear strain accumulation so that we may approximate that the Green's function is roughly constant in each interval. The normalized moment rate power spectrum

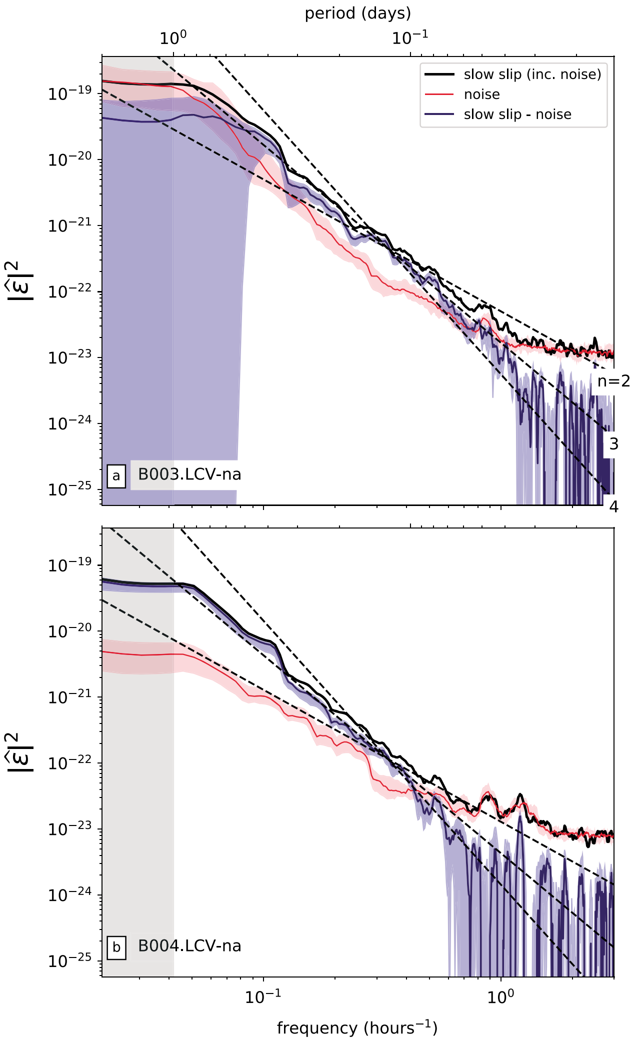

**Figure 6.** Black: Power spectra of the strain observations, averaged over the seven slow slip intervals at (a) B003 and (b) B004. Red and pink: Spectra during the noise interval sets, taken 28 to 84 days before or after the slow slip intervals. The red line indicates the median value obtained among the time shifts, and the pink shading delimits the 15th and 85th percentiles. Blue: Estimates of the true slow slip spectra: the observed slow slip spectra minus the noise spectra. The blue line marks the median, and the shading delimits the 15th to 85th percentiles. Diagonal dashed lines indicate scalings as frequency $f^{-2}$, $f^{-3}$, and $f^{-4}$, as labeled. Note that the spectra flatten at low frequencies (gray shading) because we have high-pass filtered to periods longer than 0.5 day$^{-1}$ before extracting the intervals.

$|\hat{\dot{M}}_0(f)/\bar{\dot{M}}_0|^2$ is then approximately equal to the normalized strain rate spectrum $|\hat{\dot{\varepsilon}}(f)/\bar{\dot{\varepsilon}}|^2$, where $\bar{\dot{M}}_0$ and $\bar{\dot{\varepsilon}}$ are the interval-averaged moment rate and strain rate, respectively.

To compute $|\hat{\dot{\varepsilon}}(f)/\bar{\dot{\varepsilon}}|^2$, we first numerically differentiate the strain time series to obtain strain rate and compute the power spectrum in each slow slip interval. Then we normalize by the interval's average strain rate $|\bar{\dot{\varepsilon}}|^2$. Finally, we average $|\hat{\dot{\varepsilon}}(f)/\bar{\dot{\varepsilon}}|^2$ over the seven slow slip intervals and subtract the noise spectra, which have also been normalized by the slow slip $|\bar{\dot{\varepsilon}}|^2$ values. The well-resolved portion of the normalized strain rate spectra is plotted along with the GPS-derived moment rate spectra in Figure 1.

Fits to the spectra give 90% confidence intervals on $n_s$ between 0.29 and 1.35 at B003 and between 0.80 and 1.78 at B004. The best fitting power law decays imply that the strain rate power spectra $|\hat{\dot{\varepsilon}}(f)/\bar{\dot{\varepsilon}}|^2 = 0.014f^{-0.92}$ at B003 and $0.019f^{-1.24}$ at B004, where frequency $f$ has units of day$^{-1}$. Note that the normalized power estimated at the longest well-resolved period of 1 day, 0.01 to 0.02, is within a factor of 2 of the power extracted from the GPS-based slip inversions at their shortest, well-resolved periods of 6 to 10 days. The similarity suggests that the power does not decrease systematically in the intervening frequency range.

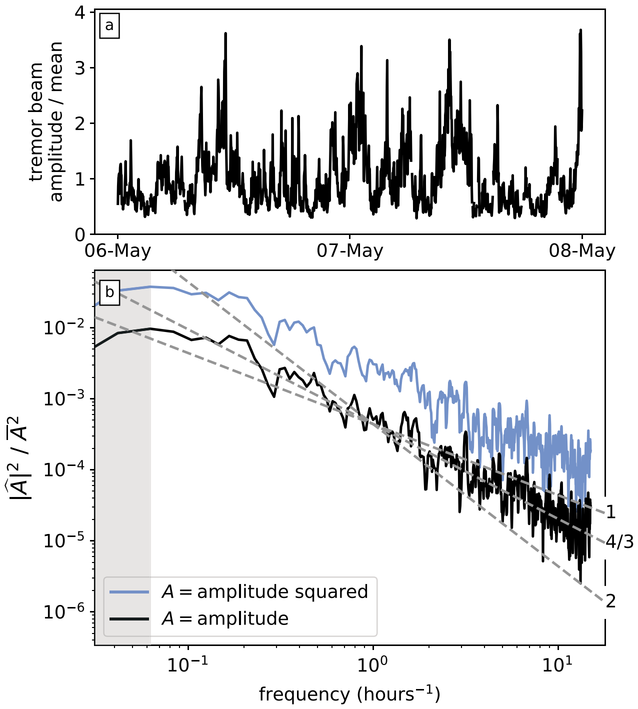

**Figure 7.** (a) Tremor amplitude estimated by Ghosh et al. (2009), observed during the May 2008 slow slip event in central Cascadia. (b) Power spectra of the tremor amplitude (black) and the squared tremor amplitude (blue), normalized by their respective means. Note that the square is computed in the time domain. Dashed gray lines mark decays as frequency$^{-2}$, frequency$^{-4/3}$, and frequency$^{-1}$. The flattening at low frequencies results from the 2-day duration of the signal and from the smoothing in the multitaper spectral estimation, which includes tapers concentrated below 0.03 hr$^{-1}$ (Slepian, 1976; Percival & Walden, 1993).

## 4. Tremor

To examine moment rate variations at much shorter periods (<1 hr), where geodetic estimates are currently unavailable, we analyze variations in tremor amplitude. The tremor amplitude we analyze was derived via beamforming by Ghosh et al. (2009). We focus on a 2-day interval shown in Figure 7a when the tremor was near the array and changes in the tremor strength are well resolved.

### 4.1. Inferring Moment Rate From Tremor Amplitude

A number of studies have shown that tremor and slip are correlated on timescales from seconds to weeks, at least in Cascadia and Japan (Ide et al., 2008; Aguiar et al., 2009; Bartlow et al., 2011; Hawthorne & Rubin, 2013c; Ide & Yabe, 2014). However, these time-averaged correlations cannot confirm that *all* variations in tremor reflect variations in the aseismic moment rate (Kostoglodov et al., 2010; Wech & Bartlow, 2014). Our tremor-based moment rate spectrum should therefore be considered only as a current best estimate and interpreted with caution.

There is also uncertainty in how we estimate the (mostly aseismic) moment rate from seismogram-derived tremor properties. In Cascadia, Hawthorne and Rubin (2013c) found that moment rate was roughly proportional to tremor envelope amplitude on timescales of 30 min to 16 hr, though they examined only modest (factor of 1.5 to 2) amplitude variations. But in Japan, Ide et al. (2008) and Ide and Yabe (2014) found that the moment rate in 20- to 200-s-long slow earthquakes tracked the power of the band-passed velocity seismograms. And the “tremor amplitude” that we analyze here was interpreted as an estimate of the *tremor* moment rate by its creators (Ghosh et al., 2009). The amplitude we analyze is the average absolute value of the 3–8 Hz stacked displacement seismogram, computed in 2-min windows.

To understand how we can best interpret the displacement absolute value, we generate some synthetic tremor in section S6. We find that the displacement absolute value scales linearly with the velocity seismogram envelope and as the square root of the velocity seismogram power, as might be expected for numerous overlapping LFEs (e.g., Ide, 2008; Gomberg, Agnew et al., 2016). If we couple the obtained envelope scaling with the moment rate-tremor envelope correlations of Hawthorne and Rubin (2013c), we infer that the aseismic moment rate should be proportional to the tremor amplitude plotted in Figure 7a. But if we couple the velocity power scaling with the moment rate-tremor power correlations of Ide et al. (2008) and Ide and Yabe (2014), we infer that the aseismic moment rate should be proportional to the square of the tremor amplitude.

### 4.2. Estimated Tremor Spectra

We therefore compute two estimates of the moment rate spectra: the spectra of the tremor amplitude and the spectra of tremor amplitude squared (where the square is in the time domain). The power spectra are shown in Figure 7b, normalized by their time-domain means. The two normalized power spectra turn out to have approximately the same frequency decay rate. We compute least-squares fits in log-log space in the 12-hr to 4-min period range, bootstrapping by frequency. The central 90% of the fits imply power spectral decays between frequency$^{-1.37}$ and frequency$^{-1.23}$ for the tremor amplitude and decays between frequency$^{-1.25}$ and frequency$^{-1.09}$ for the tremor amplitude squared.

These decay rates are consistent with the power spectral decays inferred from strain data, which implied that the moment rate power decayed as frequency$^{-n_m}$, with $n_m$ between 0.4 and 1.5. The normalized power of the tremor amplitude is also roughly consistent with the strain rate power, but the spectrum of the tremor amplitude squared plots at values a factor of a few larger. The difference in the strain power and the power of the tremor amplitude squared could imply that tremor amplitude is a better estimate of the aseismic moment rate. Or the difference could imply that the average tremor amplitude used for normalization is incorrect. The average tremor amplitude may vary on several-day timescales as slip migrates along strike, rupturing various tremor patches.

Given the uncertainties in interpreting tremor, the tremor-based moment rate spectra should be used only as a current best estimate. We nevertheless plot the spectra along with the slip inversion and strain rate spectra in Figure 1. The combined spectra, compiled from nine different slow slip events, suggest that the slow slip moment rate power

1. decays from $M_{0t}^2$ at periods longer than the slow slip event to roughly $0.01M_{0t}^2$ at periods around 10 days;
2. is unconstrained by data at periods of 1 to 10 days, but may be roughly flat since the strain rate-derived power at a 1-day period is also around 0.01 to $0.02M_{0t}^2$; and
3. decays as frequency$^{-n_m}$ at higher frequencies, where $n_m$ is estimated to be between 0.4 and 1.5 or between 1.1 and 1.4 when using the strain or tremor data, respectively.

## 5. Modeling Moment Rate Variability Created by Subevents

To understand how such a moment rate power spectrum might arise, we examine how a collection of subevents occurring within a slow slip event—including SSFs, RTRS, RTMs, VLFEs, and LFEs—could contribute to variations in moment rate at a range of timescales (e.g., Ito et al., 2007; Ide et al., 2008; Ghosh et al., 2010; Ide, 2010a; Obara, 2010; Houston et al., 2011; Peng et al., 2015). We model the moment rate in a slow slip event as the sum of two components, illustrated in Figure 8: (1, panel a) a steady background moment rate and (2, panels b–d) short-lived moment rate increases associated with subevents of various sizes. We include moment rate contributions from many small, short events (Figure 8d) and from a few large, long events (Figure 8d).

Such subevents could be driven by rupture of asperities on the plate interface or by stochastic variations in the slipping area (e.g., Ide, 2008; Ando et al., 2010; Rubin, 2011). But in this study, we will not attempt to model the subevents' physical origins. We simply assume that a fraction $F_s$ of the slow slip moment accumulates in subevents, and then we examine how the moment rate power spectrum depends on the properties of the subevent population: on the subevents' size distribution, moment-duration scaling, and moment rate evolution.

We describe the subevent population with six free parameters in section 5.1 and then illustrate how the model works with time-domain numerical simulations in section 5.2. In section 5.3, we gain more insight into the modeled spectra with analytical calculations.

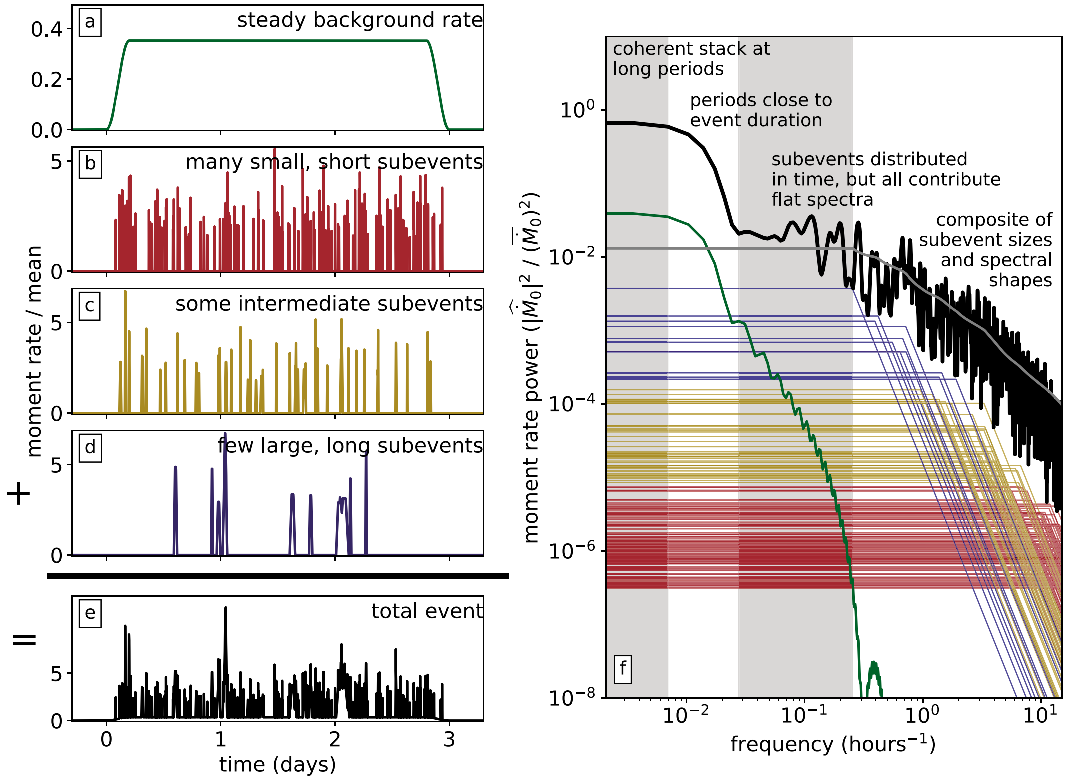

**Figure 8.** Illustration of our parameterization of a slow slip event. We construct the total slow slip moment rate (panel e) as the sum of (a) a background slip rate and (b–d) the moment rates of a population of smaller events. In panel f, the black and colored curves show the spectra of the whole event and its constituents, respectively. The gray curve shows the sum of the subevent spectra. The alternating shading and text annotations indicate four frequency ranges that result in the subevent spectra combining differently, as described in sections 5.3.1, 5.3.2, 5.3.3.1, and 5.3.3.2. Note that the subevent population and event durations are chosen only for illustration. They are not representative of Cascadia slow slip events.

### 5.1. Parameterizing the Subevent Population

To parameterize the subevent size distribution, we assume that subevent moments are drawn from a truncated Gutenberg-Richter distribution, including events up to a maximum magnitude $M_m$ (Gutenberg & Richter, 1944; Utsu, 2002). Before truncation, the number of events $N$ with moment magnitude (Hanks & Kanamori, 1979) larger than $M_W$ is

$$\log_{10} N = a - b(M_w - M_r). \tag{1}$$

Here $M_r$ is a reference magnitude, often taken to be 0 in seismicity analysis.

To parameterize the subevent durations, we assume a power law scaling between subevent duration $T$ and moment $M_0$:

$$T = CM_0^{1/m}, \tag{2}$$

where $C$ is a constant. Note that the linear moment-duration scaling proposed for slow earthquakes (e.g., Ide et al., 2007; Gao et al., 2012) would imply $m = 1$, while small earthquakes, with roughly circular areas and constant rupture speeds, typically have durations that scale as $M_0^{1/3}$ (e.g., Abercrombie, 1995; Prejean & Ellsworth, 2001; Prieto et al., 2004; Yamada et al., 2007; Gomberg, Agnew et al., 2016).

Finally, to parameterize the shape of the subevents' moment rate functions, we assume that each subevent's moment rate evolves following a boxcar function or the convolution of two or three boxcar functions.

### 5.2. Time-Domain Numerical Simulations

We use the subevent parameterization to numerically create slow slip events with a range of parameters. One illustrative simulation is shown in Figure 9. This event has 80% of its moment in subevents, which are drawn from a Gutenberg-Richter distribution with $b$ value 1 and then distributed randomly over a 35-day interval.

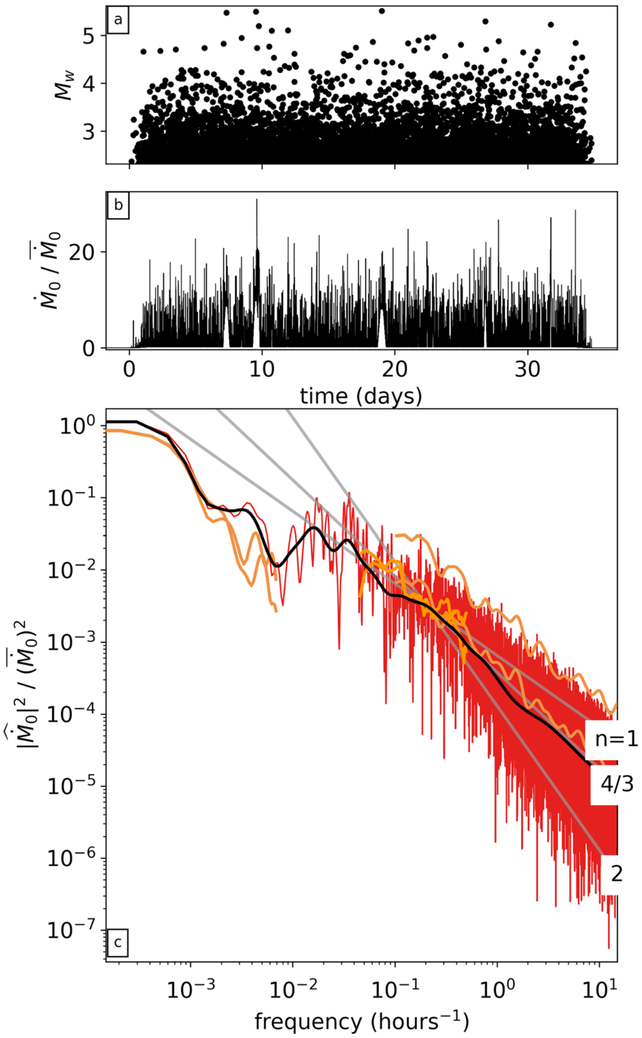

**Figure 9.** A slow slip event produced from time-domain numerical summation of subevents. (a) Magnitude (*y* axis) and timing (*x* axis) of subevents with $M_w > 2.3$. Smaller subevents are also included but not illustrated here. (b) Moment rate summed over all of the subevents, plus the modest background moment rate, divided by the average moment rate in the 35-day slow slip event. (c) Spectra of the moment rate in panel b. Spectra are computed in a 90-day interval and normalized by the average moment rate in that interval squared, leading to the value near 1 at the lowest frequencies. The red line is the original spectrum. The black line is the same spectrum, but smoothed in log-log space using a lognormal Gaussian with factor of 1.3 half width. Gray lines illustrate frequency decay with slopes of 1, 4/3, and 2, as labeled. Orange curves indicate data-derived spectra reproduced from Figure 1.

In this example, the number of subevents is chosen so that there are 20 $M_w > 4.8$ events, to roughly match the number of RTRs in Cascadia (Houston et al., 2011; Royer et al., 2015). Subevent durations are chosen to scale roughly linearly with moment ($m = 1$). Further details of the numerical computation are given in section S7.

The power spectrum of the computed total moment rate is shown in Figure 9c. It has been normalized by the time-averaged moment rate ($\bar{\dot{M}}_0$) to facilitate comparison with the GPS, strain, and tremor data, which are also plotted. The observed and modeled spectra are similar, as the parameters for this simulation were chosen to match the observations. In the simulation, the normalized moment rate power is near 1 at very low frequencies. The power initially decreases as the frequency increases but then hovers around 0.01 at frequencies between 0.01 and 0.1 hr$^{-1}$. At frequencies higher than 0.1 hr$^{-1}$, the power decays as frequency$^{-4/3}$.

We will gain more insight into the spectral shape and amplitude in the next section, via analytical calculations. But first, we perform a suite of simulations, trying *b* values of 0.6, 1, and 1.4, moment-duration scalings *m* of 0.5, 1, and 2, various maximum subevent magnitudes, and three different subevent moment rate functions (shown in Figure S19a). Several of these additional simulation results are shown in Figures S20–S25, and some of their spectra are collected in Figure 10. Note that we obtain similar normalized spectra when we extract and analyze several-day-long portions of the simulated moment rate, though the spectra are often shifted vertically by a few tens of percent because the background moment rate used for normalization varies with time (Figure S26).

In all simulations shown in Figure 10, 75% of the expected total moment is assigned to accumulate via subevents. To roughly match RTR observations, a $M_W$ 5 event is assigned a duration around 3 hours (Houston et al., 2011; Royer et al., 2015; Hawthorne et al., 2016). The *a*-value determining the total number of subevents is chosen such that there would be 30 $M_W > 5$ events in an untruncated Gutenberg-Richter distribution, but only subevents shorter than 18 hours are allowed.

### 5.3. Understanding the Spectrum: Analytical Spectral Summation

To obtain more insight into how the subevent population dictates the modeled spectrum, we divide the spectrum into four frequency ranges, illustrated in Figure 8f. We use approximations appropriate for each frequency range to obtain an analytical estimate of the spectrum. We will show that the moment rate power

1. is equal to $M_{0t}^2$ at long periods but decreases as the period gets shorter than the event duration (sections 5.3.1 and 5.3.2, equations (3) and (4)),
2. is roughly flat at periods shorter than the slow slip event but longer than the longest subevent (section 5.3.3.1, equation (8)), and
3. decreases as frequency$^{-n_m}$ at high frequencies (section 5.3.3.2, equations (10), (12), and (13)).

#### 5.3.1. Periods Longer Than the Whole Slow Slip Event: Coherent $M_{0t}^2$ Power

When we consider very low frequencies, all of the moment in the simulated slow slip event accumulates in a small portion of the period of interest (left gray shading for the toy model in Figure 8f). The moment rate function is resolvable only as a delta function, and the moment rate power spectrum is equal to the event's total moment $M_{0t}$ squared:

$$S(f \rightarrow 0) = M_{0t}^2. \tag{3}$$

Here we have defined the power spectrum $S(f)$ as $\left| \int \dot{M}(t) e^{i2\pi ft} \mathrm{d}t \right|^2$.

#### 5.3.2. Periods Comparable to the Whole Event Duration: Initial Decrease in Power

As we consider shorter periods, the moment rate becomes spread over a larger portion of the period of interest and thus starts to stack incoherently. To obtain a first-order approximation of the spectrum at these periods, we assume that the slow slip event has a boxcar-shaped moment rate function with duration $T_t$, which implies a power spectrum [equation (S16)]

$$S\left(f \approx \frac{1}{T_t}\right) = M_{0t}^2 \left( \frac{\sin\left(\pi f T_t\right)}{\pi f T_t} \right)^2. \tag{4}$$

#### 5.3.3. Periods Shorter Than the Whole Event, in Two Parts

As we consider moment rate variations at even shorter periods, which are smaller than the whole event duration, subevents appear distributed at random times throughout the cycle. In this regime, which we will divide into two frequency ranges, the power spectrum of the summed moment rate is given by the sum of the subevents' power spectra:

$$S\left(f \gtrsim \frac{1}{T_t}\right) \approx \int_0^{M_{0m}} \rho(M_0) S_i(f, M_0) \mathrm{d}M_0. \tag{5}$$

Here $\rho(M_0)$ is the number of subevents per unit moment, and $S_i(f, M_0)$ is the power spectrum of an individual subevent with moment $M_0$. The steady background moment rate contributes little power at these or higher frequencies, so we neglect it for the rest of our analysis.

The number of subevents per unit moment $\rho(M_0)$ can be estimated from the assumed Gutenberg-Richter magnitude distribution [equations (1) and (S11)]. The individual subevent spectra $S_i$ are assumed to be flat below a specified corner frequency $f_c$ and then decay as $f^{-2n}$ (black in Figure S19b), so that

$$S_i(f, M_0) = \begin{cases} M_0^2; & f < f_c \\ M_0^2 \left(\frac{f}{f_c}\right)^{-2n}; & f \geq f_c \end{cases}. \tag{6}$$

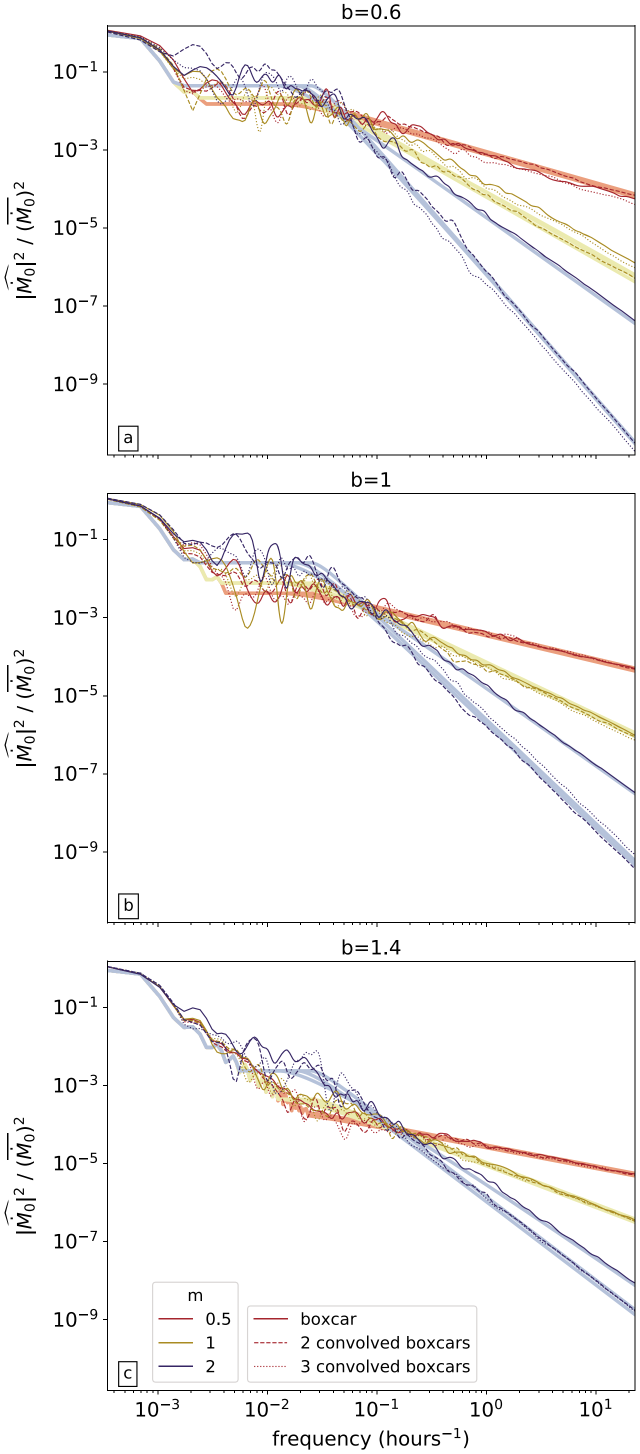

**Figure 10.** Dark solid, dashed, and dashed-dotted lines: power spectra of slow slip events constructed from subevents with a range of parameters. The line style indicates the shape of the subevent moment rate functions, and color indicates the moment-duration scaling exponent $m$ in $M \sim T^m$. The subevent magnitude distribution $b$ value is (a) 0.6, (b) 1, or (c) 1.4. Lighter but thicker lines indicate the spectra predicted from the frequency domain integration.

The high-frequency decay exponent $n$ reflects the shape of the subevent moment rate functions. For example, $n = 1$ is consistent with a boxcar function moment rate, while an $n = 2$ decay approximates the convolution of two boxcar functions.

The subevents' corner frequencies $f_c$ scale inversely with their durations, as $T^{-1}$ (e.g., Shearer, 2009). The moment-duration scaling from equation (2) thus implies

$$f_c = \frac{c_T}{T} = \frac{c_T}{C}\left(\frac{1}{M_0}\right)^{1/m}. \tag{7}$$

The constant $c_T$ is 0.22, 0.34, and 0.45 for our assumed moment rate functions, composed of one, two, and three convolved boxcar functions, respectively (Figure S19).

With these definitions, we may use equation (5) to sum the subevent spectra and thereby estimate the total event's moment rate spectrum at periods shorter than the whole slow slip event. We compute the spectra in two frequency ranges.

#### 5.3.3.1. Periods Longer Than the Longest Subevent: Flat Spectrum

At frequencies smaller than $f_m$, the corner frequency of the largest subevent, all of the subevents have flat spectra (right gray region in Figure 8f). The spectrum of the whole slow slip event is then also flat. It has value (see section S9.2)

$$S_{\text{flat}} = S\left(\frac{1}{T_t} \lesssim f < f_m\right) = \int_0^{M_{0m}} M_0^2 \rho(M_0) \mathrm{d}M_0 \tag{8}$$

$$= M_{0t}^2 F_s^2 \frac{(1-2b/3)^2}{2-2b/3}\,\frac{3}{2b}\,\frac{1}{N_e(M > M_{0m})}. \tag{9}$$

Here $M_{0t}$ is the total moment, and $N_e(M > M_{0m})$ is the number of subevents that were excluded by truncating the distribution at a maximum subevent moment $M_{0m}$. The power tends to decrease relative to $M_{0t}^2$ when $N_e$ increases—when the moment is divided into more subevents.

#### 5.3.3.2. Periods Shorter Than the Longest Subevent: Power Law Spectral Decay

At frequencies higher than the largest subevent corner frequency $f_m$, summing the subevent power spectra [equation (5)] is more complex. Some subevents have corner frequencies smaller than the frequency of interest $f$, and their spectra have already started to decay. In section S9.3, we show that the spectrum at frequencies higher than $f_m$ is

$$\begin{aligned} S(f > f_m) = S_{\text{flat}}&\left[1 - \frac{2-2b/3}{2-2n/m-2b/3}\right]\left(\frac{f}{f_m}\right)^{-m(2-2b/3)} \\ &+ S_{\text{flat}}\frac{2-2b/3}{2-2n/m-2b/3}\left(\frac{f}{f_m}\right)^{-2n} \end{aligned} \tag{10}$$

[equation (S46)] when $m(2-2b/3) \neq 2n$, and

$$S(f > f_m) = S_{\text{flat}}\left(1 + 2n\ln\left(\frac{f}{f_m}\right)\right)\left(\frac{f}{f_m}\right)^{-2n} \tag{11}$$

[equation (S46)] when $m(2-2b/3) = 2n$.

Examination of equations (10) and (11) reveals three potential spectral decay rates, depending on the values of $m$, $n$, and $b$ (see section S9.3.2 for detailed discussion). First, when $2n > m(2-2b/3)$, the power spectra decay as $f^{-n_m}$, with decay exponent

$$n_m = m(2-2b/3). \tag{12}$$

In this regime, $n_m$ is controlled only by $b$ and $m$, by the subevent size distribution and moment-duration scaling. In contrast, when $2n < m(2-2b/3)$ (as is the case for simulations with $m = 2$ and $n = 1$ in Figure 10), the total event's spectral decay is equal to the subevents' spectral decay, regardless of $m$ and $b$:

$$n_m = 2n. \tag{13}$$

When $2n = m(2-2b/3)$, the $f^{-2n}$ and $f^{-m(2-2b/3)}$ decays are equivalent, and both are accurate at very high frequencies. However, at frequencies within a factor of 10 of $f_m$, the decay rate is significantly shallower because of the $\ln(f/f_m)$ term in equation (S49).

### 5.4. A Special Case: Subevents of Subevents

An interesting special case builds from a $2n = m(2-2b/3)$ scenario. If all slow earthquakes are part of a single continuum, we may wish to model subevents in the same way as the large events: as the sum of a background moment rate and a collection of further subevents. The subevents' subevents could also contain collections of subevents, until some minimum subevent size is reached. We have so far not been able to develop an analytical understanding of the moment rate spectra of slow slip events with recursively divided subevents. However, numerical simulations presented in section S11 reveal that large events constructed from fractal subevents have power spectra that fall off roughly as $f^{-m}$ at high frequencies, regardless of the $b$ value.

## 6. Comparison of the Modeled and Observed Spectra

With our understanding of how subevents contribute to the whole event spectrum, we can choose subevent population parameters to match the spectrum derived from GPS, strain, and tremor data. We cannot, however, rigorously test the subevent model because the model requires seven free parameters to describe the subevents' size distribution ($a$, $b$, and $M_{0m}$), durations ($m$ and $C$), and moment rate functions ($n$), as well as the background moment rate ($F_s$). Not all of these parameters can be constrained with existing data. Nevertheless, we will (1) constrain the allowable subevent populations to facilitate future testing and interpretation and (2) assess the linear moment-duration scaling proposed by Ide et al. (2007) in context of the subevent model.

### 6.1. High-Frequency Decay: Implications for *b*, *m*, and *n*

The most interesting feature to match with the subevent population is the high-frequency (>1 day$^{-1}$) power spectral decay coefficient $n_m$, which is estimated to fall between 0.4 and 1.5 or between 1.1 and 1.4 when using the strain or tremor data, respectively. We can match this slope in one of three regimes, described in sections 5.3.3.2 and 5.4.

First, if $2n > m(2-2b/3)$, we can match the spectrum by selecting the magnitude distribution $b$ value and moment-duration exponent $m$ such that $m(2-2b/3) = n_m$ [equation (12)]. If $b$ is between 0.5 and 1.5, as observed for earthquakes (e.g., Kagan, 1999; Tormann et al., 2014), small slow slip events (Wech et al., 2010), and tremor migrations counts (Obara, 2012; Bletery et al., 2017), the observed $n_m$ values constrain $m$ to be between 0.25 and 1.5. Such small $m$ values, which imply a strong scaling of duration with moment, match the linear ($m = 1$) moment-duration relationship proposed as the scaling for a single slow earthquake family (Ide et al., 2007, 2008; Aguiar et al., 2009; Gao et al., 2012). The estimated $m < 1.5$ values are inconsistent with the $T^3$ moment scaling that is expected for events that grow radially outward at a constant rupture velocity and that is often observed in earthquakes smaller than the seismogenic zone width (Scholz, 1982; Abercrombie, 1995; Uchide & Ide, 2010; Gomberg, Agnew et al., 2016). The inferred $m < 1.5$ values would thus suggest that slow earthquake dynamics are different from earthquake dynamics.

On the other hand, we can match the data with a wider range of $m$ values if we allow individual subevents to have shallow spectral decay, choosing subevent properties such that $2n < m(2-2b/3)$. In this case, we can match the data by choosing $2n = n_m$ [equation (13)]: by giving the subevents the same spectral decay as the large event. We note, however, that a power spectra that decays more slowly than frequency$^{-1.5}$ is quite shallow—more shallow than for a boxcar function, which has $2n = 2$. The moment rates of subevents with such shallow decay rates would have to increase nonmonotonically to their peak values or decrease nonmonotonically to zero after their peaks.

Finally, we can match the observed spectral decay by constructing the whole slow slip event with collections of subevents, and then modeling those subevents with further collections of subevents (section 5.4). In this regime, we should pick $m$ equal to the observed $n_m$, between 0.4 and 1.5. This $m$ is again consistent with the proposed linear moment-duration proposed by Ide et al. (2007) but inconsistent with the $m = 3$ scaling expected for small events with constant rupture velocity (Gomberg, Agnew et al.,2016).

### 6.2. Extent of the Flat Spectrum: Constraints on the Longest Subevent

At periods between 1 and 10 days, the moment rate spectrum is not directly constrained by the data. However, the strain and GPS data suggest that the moment rate power is around 0.01 to $0.02M_{0t}^2$ at both of these periods, so it is possible that the spectrum is roughly flat between the two constraints.

In the subevent parameterization, the spectrum is flat at frequencies smaller than the corner frequency of the longest subevent. So to reproduce the spectrum with a population of subevents, the longest subevent should have duration of order 0.5 to 1 day.

### 6.3. RTR Rate: Constraints on $C$ and $a$

Further constraints on the subevent parameters come from observations of individual subevents. For instance, quasi-daily $M_W$ 4.8–5.1 RTRs that last several hours constrain the $a$ value of the subevent size distribution [equation (1)] and bound the coefficient $C$ in the moment-duration scaling [$T = CM_0^{1/m}$, equation (2); e.g., Houston et al., 2011; Thomas et al., 2013; Royer et al., 2015; Hawthorne et al., 2016; Peng & Rubin, 2016].

### 6.4. Minimum Moment Rates: Constraints on $F_s$

In the month-long slip inversions of Bartlow et al. (2011) and Wech and Bartlow (2014), the moment rate rarely decreases to less than half its average. Up to half of the moment rate in Cascadia events might then accumulate as “background” moment rate in our model (so $F_s \gtrsim 0.5$). In Mexico, on the other hand, stacked GPS observations imply that the moment rate is near zero outside of times with LFE bursts, suggesting that any steady moment rate would be much smaller there (Frank et al., 2017).

### 6.5. Total Moment and Short-Period Power: Constraints on $M_{0m}$, $F_s$, and $b$

We may further constrain the allowable subevent populations with two additional observations. First, most large slow slip events in Cascadia have equivalent magnitudes between $M_W$ 6.3 and 6.9 (e.g., Szeliga et al., 2008; Schmidt & Gao, 2010). Second, the power observed in the flat portion of the spectrum is of order $0.02M_{0t}^2$ when we interpolate between the GPS and strain data. To match these values, we may tune $F_s$, the maximum subevent moment $M_{0m}$, and $b$ using the model predictions from equations (8) and (S55). However, because of the unknown $b$ and $m$ values, the two observations only partially constrain the remaining unknown parameters: $F_s$, $M_{0m}$, and $b$. To fully constrain and test the subevent model, we will need additional observations of slow earthquakes and their spectra.

## 7. Discussion

In the first part of this study, we have used GPS, strain, and tremor data to estimate the moment rate power spectrum of a slow slip event in Cascadia at periods from 4 min to 100 days. The data-derived normalized spectrum can be used to test a variety of models of slow slip.

In the second part of this study, we have explored one way to parameterize slow slip events: as the sum of a background slip rate and a collection of subevents. While this parameterization cannot be conclusively tested with the data analyzed here, there are a range of subevent populations that would produce moment rate spectra consistent with the observations.

One acceptable population of subevents is of particular interest: that with a linear relationship between moment and duration. Such a linear scaling has been proposed as a model for the entire slow earthquake family—including slow slip events, RTRs, RTMs, VLFEs, and tremor—on the basis of individual slow earthquakes’ moments and durations (Ide et al., 2007, 2008; Aguiar et al., 2009; Gao et al., 2012). This weak scaling of moment with duration predicts that smaller slow earthquakes should have higher slip rates, as the scaling allows for a wide range of moments, durations, and areas, but a limited range of average moment rates. If this model is correct, and there really is a single family of slow earthquakes with a wide range of durations, it would seem likely that all these events are generated by a single deformation mechanism, which can somehow generate slip at a wide range of slip rates.

### 7.1. Possible Physical Origins for Subevents

The large complexity observed in slow slip events might reflect large heterogeneity in the plate interface region. For instance, each slow slip subevent might represent the rupture of an asperity with more unstable fault properties (Schmittbuhl et al., 2006; Aochi & Ide, 2009; Ando et al., 2010; Yabe & Ide, 2017) or the rupture of a collection of very small asperities (Ando et al., 2012; Luo & Ampuero, 2017). Each subevent could represent rupture of an individual fault within a network of subparallel faults, as are often seen in exhumed shear zones (Collettini et al., 2011; Lavier et al., 2013; Fagereng et al., 2014; Hayman & Lavier, 2014).

Variations in fault geometry could also play a role. A $M_0 \sim T$ scaling is often inferred for elongate slip events—for events that occupy the entire along-dip width and propagate steadily along strike (e.g., Heaton, 1990; Gomberg, Wech et al., 2016), as well as for the unidirectional propagation of dislocations on a range of scales (Gershenzon et al., 2011). A $M_0 \sim T$ to $T^2$ scaling can be generated on a moderately complex megathrust interface using standard rate and state friction, at least for slow slip events spanning two magnitude units (Liu, 2014; Li & Liu, 2016). This scaling range overlaps with the $m < 1.5$ scaling inferred from the data from one portion of our model's parameter space (see section 6.1). Similar "standard" friction on a small network of faults can reproduce a $M_0 \sim T$ scaling of slow slip events over a similar moment range (Romanet et al., 2017). And speed-limited rate and state friction on a moderately complex plate interface can generate events with moments that scale as $T^{1.3}$ over at least two magnitude units (Shibazaki et al., 2012).

Alternatively, slow earthquakes of various sizes could occur on a homogeneous planar fault. An approximation of speed-limited rate and state friction can give slow slip events with a wide range of sizes and moment-duration scaling $M_0{\sim}T^{1.5}$ (Colella et al., 2011). Near-velocity-neutral friction can generate events with a wide range of sizes and moments that scale with duration as $T^2/(\ln T)^{2/3}$ (Fisher et al., 1997; Ben-Zion, 2012).

### 7.2. Comparison With Other Spectral Models

Ide (2008, 2010b) and Ide and Maury (2018) modeled complex variations in slow slip moment rate as the result of a slipping area that grows and shrinks over the course of the slow slip event. They predicted a random-walk-like frequency$^{-2}$ decay for the moment rate power spectrum at high frequencies. However, the strain and tremor observations give a slightly shallower frequency$^{-n_m}$ decay. With the most appropriate analysis parameters, 90% confidence parameters on $n_m$ fall between 0.4 and 1.5 or between 1.1 and 1.4 when estimated from strain and tremor, respectively.

Our shallow decay also appears slightly inconsistent with the frictional sliding simulations of Ando et al. (2010), who modeled slip evolution on a heterogeneous fault and obtained $n_m$ slightly larger than 2. They argued that the $n_m \approx 2$ decay arose because the collection of subevents allowed for a boxcar-like moment rate in the whole event. However, given the subevent modeling performed here, it seems possible that Ando et al's (2010) model could be modified to give a shallower spectral decay if more complex heterogeneity were included.

### 7.3. Comparison With Tremor Envelope Spectrum

Ide's (2010b) model predicts a roughly linear relationship between the aseismic moment rate and the tremor envelope, implying that the tremor envelope power spectrum can be used as an estimate of the moment rate power spectrum. He was able to match the tremor envelope power spectrum in the 10- to 1,000-s range using a frequency$^{-2}$ decay coupled with a frequency$^{-0.6}$ decay for the noise envelope spectrum. It is unclear to us why our tremor-derived moment rate spectrum differs from his envelope spectra. Noise is unlikely to cause significant uncertainty for the beamforming-derived tremor amplitude obtained by Ghosh et al. (2009). A larger problem may be our and Ide's (2010b) assumption that tremor tracks the larger aseismic slip. We have considered moment rates that scale with tremor amplitude or with tremor amplitude squared and obtain similar, shallow power spectral decays for both (see section 4), but it could be that no such mapping is appropriate.

In its simplest form, our subevent modeling predicts little to no correlation between aseismic moment rate and tremor amplitude (see section S12 and Figure S18). We currently assume that subevents occur at random times, so there is no correlation between the high-frequency power, created mostly by small, short subevents, and the low-frequency moment rate variations, contributed mostly by large, long subevents.

However, if we assume that subevents are themselves composed of subevents (section 5.4), high moment rates do coincide in time with large high-frequency power, as there are more small, short events in intervals of increased moment rate. For at least part of parameter space, the high-frequency "tremor" power varies linearly with moment rate (Figures S14 and S16).

### 7.4. Comparison With LFE Rate Spectrum

As an alternative approach to estimating moment rate from tremor amplitude, we may hypothesize that LFEs occur on asperities and that the LFE occurrence rate reflects the loading rate from surrounding slow slip. In this case, the slow slip moment rate might scale linearly with LFE rate (e.g., Chestler & Creager, 2017a; Thomas et al., 2018). Frank et al. (2016) examined an individual LFE source in Guerrero, Mexico, and determined that the LFE rate power spectrum decreased roughly as frequency$^{-1}$. That decay rate is within the range of $n_m$ values that we infer from the strain data.

### 7.5. Comparison With VLFE Spectra

On the other hand, the $n_m = 0.4–1.5$ decay estimated from the strain data differs from an $n_m = 2$ decay estimated from VLFE spectra in the 0.01 to 0.025 Hz range (Takeo & Houston, 2014). We note, however, that Takeo and Houston (2014) estimated the spectrum of stacks of aligned VLFEs. Their spectrum may thus reflect the spectrum of an average individual event while ours reflects the spectrum of a number of overlapping events with different sizes.

### 7.6. Comparison With Tremor Spectra

Our power spectral decay exponent $n_m \approx 1$ is also slightly smaller than those estimated at higher frequencies, in the 1–20 Hz tremor band. An *amplitude* spectral decay exponent $n$ (to be compared with $n_m/2$) close to 1 has been inferred for a number of tremor observations (Ide et al., 2007; Rubinstein et al., 2007; Shelly et al., 2007). Even higher-amplitude decay exponents $n$ of 2 to 3, more similar to normal earthquakes, have also been inferred (Fletcher & McGarr, 2011; Zhang et al., 2011). However, tremor spectra are difficult to estimate for several reasons: because the well-resolved frequency band is limited, LFE corner frequencies are close to or within that frequency band, and attenuation estimates are uncertain. Local earthquakes may or may not serve as effective empirical Green's functions (Fletcher & McGarr, 2011; Zhang et al., 2011; Gomberg et al., 2012; Bostock et al., 2017).

### 7.7. LFE Magnitudes and Durations

Tremor is composed mostly of $M_W$ 1 to 3 LFEs with durations around 0.2 to 0.7 s (Shelly et al., 2006, 2007; Zhang et al., 2011; Bostock et al., 2015; Thomas et al., 2016; Chestler & Creager, 2017a). These average LFE moments and durations are consistent with the linear moment-duration scaling proposed for the whole slow earthquake family (Ide et al., 2007; Ide, 2014). However, the moment-duration scaling of events within the LFE band appears different. Bostock et al. (2015) estimated just a 10% change in LFE duration for a factor of 10 change in moment.

The size distribution of LFEs also appears inconsistent with the $b \approx 1$ Gutenberg-Richter distribution we have assumed to model the slow slip spectrum. LFE magnitude distributions are often found to be more consistent with an exponential distribution. They give $b > 4$ when modeled with a power law distribution (Watanabe et al., 2007; Shelly & Hardebeck, 2010; Chamberlain et al., 2014; Sweet et al., 2014; Bostock et al., 2015; Chestler & Creager, 2017a).

These indications of a characteristic LFE size, along with the $n > 1$ tremor spectra, may indicate that it is incorrect to model slow earthquakes across a wide frequency band with a single physical mechanism. As noted in section 1, slow slip is largely controlled by an aseismic rheology, but tremor's slip speeds are fast enough that seismic radiation may play an important role in the event's evolution, and the slow slip rheology may be irrelevant for tremor.

Alternatively, the apparently characteristic LFE size could imply that slow earthquakes are governed by material heterogeneity. It may be that most of the tremor detected so far comes from a particular set of asperities that tend to generate 0.5-s-long $M_W$ 1–2 events (e.g., Ghosh et al., 2012; Armbruster et al., 2014; Sweet et al., 2014; Chestler & Creager, 2017b). Slightly longer or shorter slow earthquakes could occur on different asperities or fault segments that we have not yet identified. Such asperity-controlled slow earthquakes would imply an important role for scale-dependent fault properties in determining how fast each fault segment slips.

## 8. Conclusions

Our analysis of GPS, strain, and tremor data compiled from nine slow slip events in Cascadia suggests that the moment rate power spectra (1) decay from $M_{0t}^2$ at long periods to of order $0.01M_{0t}^2$ at periods of 10 days, (2) are poorly constrained by data but potentially flat at frequencies between 0.1 and 1 day$^{-1}$, and (3) decay as frequency$^{-n_m}$ at frequencies of 1 day$^{-1}$ to 0.25 min$^{-1}$, where $n_m$ is between 0.4 and 1.5 when estimated from strain and between 1.1 and 1.4 when estimated from tremor.

We obtain similar spectra shapes when we model slow slip events as the sum of a background rate and a collection of subevents. Depending on the portion of parameter space, the high-frequency spectral falloff

$n_m$ is controlled either by the frequency decay of individual subevents or by the population's $b$ value and moment-duration scaling $m$.

There are not enough observations for us to rigorously test our subevent model, but if we assume that the latter portion of parameter space is correct, we obtain scalings $m$ between 0.25 and 1.5 when we compare the model with the data. This range is consistent with the linear ($m = 1$) moment-duration scaling proposed for a single slow earthquake family spanning a wide range of durations and slip speeds (e.g., Ide et al., 2007).

**Acknowledgments**

We are grateful to A. Ghosh for providing the tremor beamforming data from the 2008 slow slip event. The strain data used come from Plate Boundary Observatory borehole strainmeters, operated by UNAVCO for EarthScope and supported by the National Science Foundation grants EAR-0350028 and EAR-0732947. The data were obtained from UNAVCO via IRIS. We are grateful to two anonymous reviewers whose comments improved the manuscript. This work was funded in part by NERC grant NE/P012507/1.

## References

Abercrombie, R. E. (1995). Earthquake source scaling relationships from −1 to 5 ML using seismograms recorded at 2.5-km depth. *Journal of Geophysical Research*, *100*(B12), 24,015–24,036. https://doi.org/10.1029/95JB02397

Aguiar, A. C., Melbourne, T. I., & Scrivner, C. W. (2009). Moment release rate of Cascadia tremor constrained by GPS. *Journal of Geophysical Research*, *114*, B00A05. https://doi.org/10.1029/2008JB005909

Ando, R., Nakata, R., & Hori, T. (2010). A slip pulse model with fault heterogeneity for low-frequency earthquakes and tremor along plate interfaces. *Geophysical Research Letters*, *37*, L10310. https://doi.org/10.1029/2010GL043056

Ando, R., Takeda, N., & Yamashita, T. (2012). Propagation dynamics of seismic and aseismic slip governed by fault heterogeneity and Newtonian rheology. *Journal of Geophysical Research*, *117*, B11308. https://doi.org/10.1029/2012JB009532

Aochi, H., & Ide, S. (2009). Complexity in earthquake sequences controlled by multiscale heterogeneity in fault fracture energy. *Journal of Geophysical Research*, *114*, B03305. https://doi.org/10.1029/2008JB006034

Armbruster, J. G., Kim, W.-Y., & Rubin, A. M. (2014). Accurate tremor locations from coherent *S* and *P* waves. *Journal of Geophysical Research: Solid Earth*, *119*, 5000–5013. https://doi.org/10.1002/2014JB011133

Asano, Y., Obara, K., Matsuzawa, T., Hirose, H., & Ito, Y. (2015). Possible shallow slow slip events in Hyuga-nada, Nankai subduction zone, inferred from migration of very low frequency earthquakes. *Geophysical Research Letters*, *42*, 331–338. https://doi.org/10.1002/2014GL062165

Bartlow, N. M., Miyazaki, S., Bradley, A. M., & Segall, P. (2011). Space-time correlation of slip and tremor during the 2009 Cascadia slow slip event. *Geophysical Research Letters*, *38*, L18309. https://doi.org/10.1029/2011GL048714

Ben-Zion, Y. (2012). Episodic tremor and slip on a frictional interface with critical zero weakening in elastic solid. *Geophysical Journal International*, *189*(2), 1159–1168. https://doi.org/10.1111/j.1365-246.2012.05422.x

Bishop, C. M. (2006). *Pattern recognition and machine learning*. New York: Springer.

Bletery, Q., Thomas, A. M., Hawthorne, J. C., Skarbek, R. M., Rempel, A. W., & Krogstad, R. D. (2017). Characteristics of secondary slip fronts associated with slow earthquakes in Cascadia. *Earth and Planetary Science Letters*, *463*, 212–220. https://doi.org/10.1016/j.epsl.2017.01.046

Bostock, M. G., Thomas, A. M., Rubin, A. M., & Christensen, N. I. (2017). On corner frequencies, attenuation, and low-frequency earthquakes. *Journal of Geophysical Research: Solid Earth*, *122*, 543–557. https://doi.org/10.1002/2016JB013405

Bostock, M. G., Thomas, A. M., Savard, G., Chuang, L., & Rubin, A. M. (2015). Magnitudes and moment-duration scaling of low-frequency earthquakes beneath southern Vancouver Island. *Journal of Geophysical Research: Solid Earth*, *120*, 6329–6350. https://doi.org/10.1002/2015JB012195

Chamberlain, C. J., Shelly, D. R., Townend, J., & Stern, T. A. (2014). Low-frequency earthquakes reveal punctuated slow slip on the deep extent of the Alpine Fault, New Zealand. *Geochemistry, Geophysics, Geosystems*, *15*, 2984–2999. https://doi.org/10.1002/2014GC005436

Chestler, S. R., & Creager, K. C. (2017a). Evidence for a scale-limited low-frequency earthquake source process. *Journal of Geophysical Research*, *122*, 3099–3114. https://doi.org/10.1002/2016JB013717

Chestler, S. R., & Creager, K. C. (2017b). A model for low-frequency earthquake slip. *Geochemistry, Geophysics, Geosystems*, *18*, 4690–4708. https://doi.org/10.1002/2017GC007253

Colella, H. V., Dieterich, J. H., & Richards-Dinger, K. B. (2011). Multi-event simulations of slow slip events for a Cascadia-like subduction zone. *Geophysical Research Letters*, *38*, L16312. https://doi.org/10.1029/2011GL048817

Colella, H. V., Dieterich, J. H., Richards-Dinger, K., & Rubin, A. M. (2012). Complex characteristics of slow slip events in subduction zones reproduced in multi-cycle simulations. *Geophysical Research Letters*, *39*, L20312. https://doi.org/10.1029/2012GL053276

Collettini, C., Niemeijer, A., Viti, C., Smith, S. A., & Marone, C. (2011). Fault structure, frictional properties and mixed-mode fault slip behavior. *Earth and Planetary Science Letters*, *311*(3-4), 316–327. https://doi.org/10.1016/j.epsl.2011.09.020

Dragert, H., & Wang, K. (2011). Temporal evolution of an episodic tremor and slip event along the northern Cascadia margin. *Journal of Geophysical Research*, *116*, B12406. https://doi.org/10.1029/2011JB008609

Dragert, H., Wang, K. L., & James, T. S. (2001). A silent slip event on the deeper Cascadia subduction interface. *Science*, *292*(5521), 1525–1528. https://doi.org/10.1126/science.1060152

Fagereng, Å., Hillary, G. W. B., & Diener, J. F. A. (2014). Brittle-viscous deformation, slow slip, and tremor. *Geophysical Research Letters*, *41*, 4159–4167. https://doi.org/10.1002/2014GL060433

Fisher, D. S., Dahmen, K., Ramanathan, S., & Ben-Zion, Y. (1997). Statistics of earthquakes in simple models of heterogeneous faults. *Physical Review Letters*, *78*(25), 4885–4888. https://doi.org/10.1103/PhysRevLett.78.4885

Fletcher, J. B., & McGarr, A. (2011). Moments, magnitudes, and radiated energies of non-volcanic tremor near Cholame, CA, from ground motion spectra at UPSAR. *Geophysical Research Letters*, *38*, L16314. https://doi.org/10.1029/2011GL048636

Frank, W. B., Rousset, B., Lasserre, C., & Campillo, M. (2017). Revealing the cascade of slow transients behind a large slow slip event. In *JpGU-AGU Joint Meeting*. Chiba, Japan.

Frank, W. B., Shapiro, N. M., Husker, A. L., Kostoglodov, V., Gusev, A. A., & Campillo, M. (2016). The evolving interaction of low-frequency earthquakes during transient slip. *Science Advances*, *2*(4), E1501616. https://doi.org/10.1126/sciadv.1501616

Frank, W. B., Shapiro, N. M., Husker, A. L., Kostoglodov, V., Romanenko, A., & Campillo, M. (2014). Using systematically characterized low-frequency earthquakes as a fault probe in Guerrero, Mexico. *Journal of Geophysical Research: Solid Earth*, *119*, 7686–7700. https://doi.org/10.1002/2014JB011457

Fu, Y., & Freymueller, J. T. (2013). Repeated large slow slip events at the southcentral Alaska subduction zone. *Earth and Planetary Science Letters*, *375*, 303–311. https://doi.org/10.1016/j.epsl.2013.05.049

Gao, H., Schmidt, D. A., & Weldon, R. J. (2012). Scaling relationships of source parameters for slow slip events. *Bulletin of the Seismological Society of America*, *102*(1), 352–360. https://doi.org/10.1785/0120110096

Gershenzon, N. I., Bambakidis, G., Hauser, E., Ghosh, A., & Creager, K. C. (2011). Episodic tremors and slip in Cascadia in the framework of the Frenkel-Kontorova model. *Geophysical Research Letters*, *38*, L01309. https://doi.org/10.1029/2010GL045225

Ghosh, A., Huesca-Pérez, E., Brodsky, E., & Ito, Y. (2015). Very low frequency earthquakes in Cascadia migrate with tremor. *Geophysical Research Letters*, *42*, 3228–3232. https://doi.org/10.1002/2015GL063286

Ghosh, A., Vidale, J. E., Sweet, J. R., Creager, K. C., & Wech, A. G. (2009). Tremor patches in Cascadia revealed by seismic array analysis. *Geophysical Research Letters*, *36*, L17316. https://doi.org/10.1029/2009GL039080

Ghosh, A., Vidale, J. E., Sweet, J. R., Creager, K. C., Wech, A. G., Houston, H., & Brodsky, E. E. (2010). Rapid, continuous streaking of tremor in Cascadia. *Geochemistry, Geophysics, Geosystems*, *11*, Q12010. https://doi.org/10.1029/2010GC003305

Ghosh, A., Vidale, J. E., & Creager, K. C. (2012). Tremor asperities in the transition zone control evolution of slow earthquakes. *Journal of Geophysical Research*, *117*, B10301. https://doi.org/10.1029/2012JB009249

Gomberg, J., Agnew, D. C., & Schwartz, S. Y. (2016). Alternative source models of very low frequency events. *Journal of Geophysical Research: Solid Earth*, *121*, 6722–6740. https://doi.org/10.1002/2016JB013001

Gomberg, J., Creager, K., Sweet, J., Vidale, J., Ghosh, A., & Hotovec, A. (2012). Earthquake spectra and near-source attenuation in the Cascadia subduction zone. *Journal of Geophysical Research*, *117*, B05312. https://doi.org/10.1029/2011JB009055

Gomberg, J., Wech, A., Creager, K., Obara, K., & Agnew, D. (2016). Reconsidering earthquake scaling. *Geophysical Research Letters*, *43*, 6243–6251. https://doi.org/10.1002/2016GL069967

Gutenberg, B., & Richter, C. F. (1944). Frequency of earthquakes in California. *Bulletin of the Seismological Society of America*, *34*(4), 185–188.

Hanks, T. C., & Kanamori, H. (1979). A moment magnitude scale. *Journal of Geophysical Research*, *84*(5), 2348–2350. https://doi.org/10.1029/JB084iB05p02348

Hart, R. H. G., Gladwin, M. T., Gwyther, R. L., Agnew, D. C., & Wyatt, F. K. (1996). Tidal calibration of borehole strain meters: Removing the effects of small-scale inhomogeneity. *Journal of Geophysical Research*, *101*(B11), 25,553–25,571. https://doi.org/10.1029/96JB02273

Hawthorne, J. C., & Rubin, A. M. (2010). Tidal modulation of slow slip in Cascadia. *Journal of Geophysical Research*, *115*, B09406. https://doi.org/10.1029/2010JB007502

Hawthorne, J. C., & Rubin, A. M. (2013a). Tidal modulation and back-propagating fronts in slow slip events simulated with a velocity-weakening to velocity-strengthening friction law. *Journal of Geophysical Research: Atmospheres*, *118*, 1216–1239. https://doi.org/10.1002/jgrb.50107

Hawthorne, J. C., & Rubin, A. M. (2013b). Laterally propagating slow slip events in a rate and state friction model with a velocity-weakening to velocity-strengthening transition. *Journal of Geophysical Research: Solid Earth*, *118*, 3785–3808. https://doi.org/10.1002/jgrb.50261

Hawthorne, J. C., & Rubin, A. M. (2013c). Short-time scale correlation between slow slip and tremor in Cascadia. *Journal of Geophysical Research: Solid Earth*, *118*, 1316–1329. https://doi.org/10.1002/jgrb.50103

Hawthorne, J. C., Bostock, M. G., Royer, A. A., & Thomas, A. M. (2016). Variations in slow slip moment rate associated with rapid tremor reversals in Cascadia. *Geochemistry, Geophysics, Geosystems*, *17*, 4899–4919. https://doi.org/10.1002/2016GC006489

Hayman, N. W., & Lavier, L. L. (2014). The geologic record of deep episodic tremor and slip. *Geology*, *42*(3), 195–198. https://doi.org/10.1130/G34990.1

Heaton, T. H. (1990). Evidence for and implications of self-healing pulses of slip in earthquake rupture. *Physics of the Earth and Planetary Interiors*, *64*(1), 1–20. https://doi.org/10.1016/0031-9201(90)90002-F

Heki, K., & Kataoka, T. (2008). On the biannually repeating slow-slip events at the Ryukyu Trench, southwestern Japan. *Journal of Geophysical Research*, *113*, B11402. https://doi.org/10.1029/2008JB005739

Hodgkinson, K., Langbein, J., Henderson, B., Mencin, D., & Borsa, A. (2013). Tidal calibration of Plate Boundary Observatory borehole strainmeters. *Journal of Geophysical Research: Solid Earth*, *118*, 447–458. https://doi.org/10.1029/2012JB009651

Houston, H., Delbridge, B. G., Wech, A. G., & Creager, K. C. (2011). Rapid tremor reversals in Cascadia generated by a weakened plate interface. *Nature Geoscience*, *4*(6), 404–409. https://doi.org/10.1038/ngeo1157

Ide, S. (2008). A Brownian walk model for slow earthquakes. *Geophysical Research Letters*, *35*, L17301. https://doi.org/10.1029/2008GL034821

Ide, S. (2010a). Striations, duration, migration and tidal response in deep tremor. *Nature*, *466*(7304), 356–359. https://doi.org/10.1038/nature09251

Ide, S. (2010b). Quantifying the time function of nonvolcanic tremor based on a stochastic model. *Journal of Geophysical Research*, *115*, B08313. https://doi.org/10.1029/2009JB000829

Ide, S. (2014). Modeling fast and slow earthquakes at various scales. *Proceedings of the Japan Academy, Series B*, *90*(8), 259–277. https://doi.org/10.2183/pjab.90.259

Ide, S., & Yabe, S. (2014). Universality of slow earthquakes in the very low frequency band. *Geophysical Research Letters*, *41*, 2786–2793. https://doi.org/10.1002/2014GL059712

Ide, S., Beroza, G. C., Shelly, D. R., & Uchide, T. (2007). A scaling law for slow earthquakes. *Nature*, *447*(7140), 76–79. https://doi.org/10.1038/nature05780

Ide, S., Imanishi, K., Yoshida, Y., Beroza, G. C., & Shelly, D. R. (2008). Bridging the gap between seismically and geodetically detected slow earthquakes. *Geophysical Research Letters*, *35*, L10305. https://doi.org/10.1029/2008GL034014

Ide, S., & Maury, J. (2018). Seismic moment, seismic energy, and source duration of slow earthquakes: Application of Brownian slow earthquake model to three major subduction zones. *Geophysical Research Letters*, *45*. https://doi.org/10.1002/2018GL077461

Ito, Y., Obara, K., Shiomi, K., Sekine, S., & Hirose, H. (2007). Slow earthquakes coincident with episodic tremors and slow slip events. *Science*, *315*(5811), 503–506. https://doi.org/10.1126/science.1134454

Ji, K. H., & Herring, T. A. (2013). A method for detecting transient signals in GPS position time-series: Smoothing and principal component analysis. *Geophysical Journal International*, *193*(1), 171–186. https://doi.org/10.1093/gji/ggt003

Kagan, Y. Y. (1999). Universality of the seismic moment-frequency relation. *SpringerLink*, 537–573. https://doi.org/10.1007/978-3-0348-8677-2_16

Kao, H., Shan, S.-J., Rogers, G., & Dragert, H. (2007). Migration characteristics of seismic tremors in the northern Cascadia margin. *Geophysical Research Letters*, *34*, L03304. https://doi.org/10.1029/2006GL028430

Kositsky, A. P., & Avouac, J.-P. (2010). Inverting geodetic time series with a principal component analysis-based inversion method. *Journal of Geophysical Research*, *115*, B03401. https://doi.org/10.1029/2009JB006535

Kostoglodov, V., Husker, A., Shapiro, N. M., Payero, J. S., Campillo, M., Cotte, N., & Clayton, R. (2010). The 2006 slow slip event and nonvolcanic tremor in the Mexican subduction zone. *Geophysical Research Letters*, *37*, L24301. https://doi.org/10.1029/2010GL045424

Krogstad, R. (2016). Kinematic constraints on tremor and slow slip in Cascadia and implications for fault properties (PhD thesis). U. Oregon.

Langbein, J. (2004). Noise in two-color electronic distance meter measurements revisited. *Journal of Geophysical Research*, *109*, B04406. https://doi.org/10.1029/2003JB002819

Langbein, J. (2010). Computer algorithm for analyzing and processing borehole strainmeter data. *Computers & Geosciences*, *36*(5), 611–619. https://doi.org/10.1016/j.cageo.2009.08.011

Lavier, L. L., Bennett, R. A., & Duddu, R. (2013). Creep events at the brittle ductile transition. *Geochemistry, Geophysics, Geosystems*, *14*, 3334–3351. https://doi.org/10.1002/ggge.20178

Li, D., & Liu, Y. (2016). Spatiotemporal evolution of slow slip events in a nonplanar fault model for northern Cascadia subduction zone. *Journal of Geophysical Research: Solid Earth*, *121*, 6828–6845. https://doi.org/10.1002/2016JB012857

Liu, Y. (2014). Source scaling relations and along-strike segmentation of slow slip events in a 3-D subduction fault model. *Journal of Geophysical Research: Solid Earth*, *119*, 6512–6533. https://doi.org/10.1002/2014JB011144

Liu, Y. J., & Rice, J. R. (2005). Aseismic slip transients emerge spontaneously in three-dimensional rate and state modeling of subduction earthquake sequences. *Journal of Geophysical Research*, *110*, B08307. https://doi.org/10.1029/2004JB003424

Liu, Y. J., & Rice, J. R. (2007). Spontaneous and triggered aseismic deformation transients in a subduction fault model. *Journal of Geophysical Research*, *112*, B09404. https://doi.org/10.1029/2007JB004930

Luo, Y., & Ampuero, J.-P. (2017). Tremor migration patterns and the collective behavior of deep asperities mediated by creep. *EarthArXiv*. https://doi.org/10.17605/OSF.IO/MBCAV

Matsuzawa, T., Obara, K., & Maeda, T. (2009). Source duration of deep very low frequency earthquakes in western Shikoku, Japan. *Journal of Geophysical Research*, *114*, B00A11. https://doi.org/10.1029/2008JB006044

McCrory, P. A., Blair, J. L., Waldhauser, F., & Oppenheimer, D. H. (2012). Juan de Fuca slab geometry and its relation to Wadati-Benioff zone seismicity. *Journal of Geophysical Research*, *117*, B09306. https://doi.org/10.1029/2012JB009407

Miyazaki, S., Segall, P., McGuire, J. J., Kato, T., & Hatanaka, Y. (2006). Spatial and temporal evolution of stress and slip rate during the 2000 Tokai slow earthquake. *Journal of Geophysical Research*, *111*, B03409. https://doi.org/10.1029/2004JB003426

Nakata, R., Ando, R., Hori, T., & Ide, S. (2011). Generation mechanism of slow earthquakes: Numerical analysis based on a dynamic model with brittle-ductile mixed fault heterogeneity. *Journal of Geophysical Research*, *116*, B08308. https://doi.org/10.1029/2010JB008188

Obara, K. (2002). Nonvolcanic deep tremor associated with subduction in southwest Japan. *Science*, *296*(5573), 1679–1681. https://doi.org/10.1126/science.1070378

Obara, K. (2010). Phenomenology of deep slow earthquake family in southwest Japan: Spatiotemporal characteristics and segmentation. *Journal of Geophysical Research*, *115*, B00A25. https://doi.org/10.1029/2008JB006048

Obara, K. (2012). Depth-dependent mode of tremor migration beneath Kii Peninsula, Nankai subduction zone. *Geophysical Research Letters*, *39*, L10308. https://doi.org/10.1029/2012GL051420

Okada, Y. (1985). Surface deformation due to shear and tensile faults in a half-space. *Bulletin of the Seismological Society of America*, *75*(4), 1135–1154.

Peng, Y., & Rubin, A. M. (2016). High-resolution images of tremor migrations beneath the Olympic Peninsula from stacked array of arrays seismic data. *Geochemistry, Geophysics, Geosystems*, *17*, 587–601. https://doi.org/10.1002/2015GC006141

Peng, Y., Rubin, A. M., Bostock, M. G., & Armbruster, J. G. (2015). High-resolution imaging of rapid tremor migrations beneath southern Vancouver Island using cross-station cross correlations. *Journal of Geophysical Research: Solid Earth*, *120*, 4317–4332. https://doi.org/10.1002/2015JB011892

Peng, Z., & Gomberg, J. (2010). An integrated perspective of the continuum between earthquakes and slow-slip phenomena. *Nature Geoscience*, *3*(9), 599–607. https://doi.org/10.1038/ngeo940

Percival, D. B., & Walden, A. T. (1993). *Spectral analysis for physical applications* (1st ed.). Cambridge, UK: Cambridge University Press.

Prejean, S. G., & Ellsworth, W. L. (2001). Observations of earthquake source parameters at 2 km depth in the Long Valley caldera, eastern California. *Bulletin of the Seismological Society of America*, *91*(2), 165–177. https://doi.org/10.1785/0120000079

Press, W. H. (2007). *Numerical recipes 3rd edition: The art of scientific computing*. Cambridge, UK: Cambridge University Press.

Prieto, G. A., Shearer, P. M., Vernon, F. L., & Kilb, D. (2004). Earthquake source scaling and self-similarity estimation from stacking $P$ and $S$ spectra. *Journal of Geophysical Research*, *109*, B08310. https://doi.org/10.1029/2004JB003084

Rangelova, E., van der Wal, W., Braun, A., Sideris, M. G., & Wu, P. (2007). Analysis of gravity recovery and climate experiment time-variable mass redistribution signals over North America by means of principal component analysis. *Journal of Geophysical Research*, *112*, F03002. https://doi.org/10.1029/2006JF000615

Rice, J. R. (1993). Spatio-temporal complexity of slip on a fault. *Journal of Geophysical Research*, *98*, 9885–9907. https://doi.org/10.1029/93JB00191

Roeloffs, E. (2010). Tidal calibration of Plate Boundary Observatory borehole strainmeters: Roles of vertical and shear coupling. *Journal of Geophysical Research*, *115*, B06405. https://doi.org/10.1029/2009JB006407

Roeloffs, E. (2015). Constraining aseismic slip in the Cascadia subduction zone with Plate Boundary Observatory borehole strainmeters in northern Oregon. In *AGU Fall Meeting* (pp. S31A–2723).

Romanet, P., Bhat, H. S, Jolivet, R., & Madariaga, R. (2017). Fast and slow earthquakes emerge due to fault geometrical complexity, arXiv:1709.10336[physics].

Royer, A. A., Thomas, A. M., & Bostock, M. G. (2015). Tidal modulation and triggering of low-frequency earthquakes in northern Cascadia. *Journal of Geophysical Research: Solid Earth*, *120*, 384–405. https://doi.org/10.1002/2014JB011430

Rubin, A. M. (2011). Designer friction laws for bimodal slow slip propagation speeds. *Geochemistry, Geophysics, Geosystems*, *12*, Q04007. https://doi.org/10.1029/2010GC003386

Rubin, A. M., & Ampuero, J. P. (2005). Earthquake nucleation on (aging) rate and state faults. *Journal of Geophysical Research*, *110*, B11312. https://doi.org/10.1029/2005JB003686

Rubin, A. M., & Armbruster, J. G. (2013). Imaging slow slip fronts in Cascadia with high precision cross-station tremor locations. *Geochemistry, Geophysics, Geosystems*, *14*, 5371–5392. https://doi.org/10.1002/2013GC005031

Rubinstein, J. L., Vidale, J. E., Gomberg, J., Bodin, P., Creager, K. C., & Malone, S. D. (2007). Non-volcanic tremor driven by large transient shear stresses. *Nature*, *448*(7153), 579–582. https://doi.org/10.1038/nature06017

Ryberg, T., Haberland, C., Fuis, G. S., Ellsworth, W. L., & Shelly, D. R. (2010). Locating non-volcanic tremor along the San Andreas Fault using a multiple array source imaging technique. *Geophysical Journal International*, *183*, 1485–1500. https://doi.org/10.1111/j.1365-246.2010.04805.x

Schmidt, D. A., & Gao, H. (2010). Source parameters and time-dependent slip distributions of slow slip events on the Cascadia subduction zone from 1998 to 2008. *Journal of Geophysical Research*, *115*, B00A18. https://doi.org/10.1029/2008JB006045

Schmittbuhl, J., Chambon, G., Hansen, A., & Bouchon, M. (2006). Are stress distributions along faults the signature of asperity squeeze?*Geophysical Research Letters*, *33*, L13307. https://doi.org/10.1029/2006GL025952

Scholz, C. H. (1982). Scaling laws for large earthquakes: Consequences for physical models. *Bulletin of the Seismological Society of America*, *72*(1), 1–14.

Segall, P., & Matthews, M. (1997). Time dependent inversion of geodetic data. *Journal of Geophysical Research*, *102*(B10), 22,391–22,409. https://doi.org/10.1029/97JB01795

Segall, P., Rubin, A. M., Bradley, A. M., & Rice, J. R. (2010). Dilatant strengthening as a mechanism for slow slip events. *Journal of Geophysical Research*, *115*, B12305. https://doi.org/10.1029/2010JB007449

Shearer, P. (2009). *Introduction to seismology, 2 ed*. Cambridge, UK: Cambridge University Press.

Shelly, D. R. (2010). Migrating tremors illuminate complex deformation beneath the seismogenic San Andreas Fault. *Nature*, *463*(7281), 648–652. https://doi.org/10.1038/nature08755

Shelly, D. R., & Hardebeck, J. L. (2010). Precise tremor source locations and amplitude variations along the lower-crustal central San Andreas Fault. *Geophysical Research Letters*, *37*, L14301. https://doi.org/10.1029/2010GL043672

Shelly, D. R., Beroza, G. C., & Ide, S. (2007). Non-volcanic tremor and low-frequency earthquake swarms. *Nature*, *446*(7133), 305–307. https://doi.org/10.1038/nature05666

Shelly, D. R., Beroza, G. C., Ide, S., & Nakamula, S. (2006). Low-frequency earthquakes in Shikoku, Japan, and their relationship to episodic tremor and slip. *Nature*, *442*(7099), 188–191. https://doi.org/10.1038/nature04931

Shibazaki, B., & Shimamoto, T. (2007). Modelling of short-interval silent slip events in deeper subduction interfaces considering the frictional properties at the unstable-stable transition regime. *Geophysical Journal International*, *171*(1), 191–205. https://doi.org/10.1111/j.1365-246.2007.03434.x

Shibazaki, B., Obara, K., Matsuzawa, T., & Hirose, H. (2012). Modeling of slow slip events along the deep subduction zone in the Kii Peninsula and Tokai regions, southwest Japan. *Journal of Geophysical Research*, *117*, B06311. https://doi.org/10.1029/2011JB009083

Slepian, D. (1976). On bandwidth. *Proceedings of the IEEE*, *64*(3), 292–300. https://doi.org/10.1109/PROC.1976. 10110

Sun, W.-F., Peng, Z., Lin, C.-H., & Chao, K. (2015). Detecting deep tectonic tremor in Taiwan with a dense array. *Bulletin of the Seismological Society of America*, *105*(3), 1349–1358. https://doi.org/10.1785/0120140258

Sweet, J. R., Creager, K. C., & Houston, H. (2014). A family of repeating low-frequency earthquakes at the downdip edge of tremor and slip. *Geochemistry, Geophysics, Geosystems*, *15*, 3713–3721. https://doi.org/10.1002/2014GC005449

Szeliga, W., Melbourne, T., Santillan, M., & Miller, M. (2008). GPS constraints on 34 slow slip events within the Cascadia subduction zone, 1997–2005. *Journal of Geophysical Research*, *113*, B04404. https://doi.org/10.1029/2007JB004948

Takeo, A., & Houston, H. (2014). Frequency-dependent moment release of very low frequency earthquakes in the Cascadia subduction zone. In *AGU Fall Meeting Abstracts* (pp. S51E–07). San Francisco, CA.

Thomas, A. M., Beroza, G. C., & Shelly, D. R. (2016). Constraints on the source parameters of low-frequency earthquakes on the San Andreas Fault. *Geophysical Research Letters*, *43*, 1464–1471. https://doi.org/10.1002/2015GL067173

Thomas, A. M., Beeler, N. M., Bletery, Q., Burgmann, R., & Shelly, D. R. (2018). Using low-frequency earthquake families on the San Andreas Fault as deep creepmeters. *Journal of Geophysical Research: Solid Earth*, *123*, 457–475. https://doi.org/10.1002/2017JB014404

Thomas, T. W., Vidale, J. E., Houston, H., Creager, K. C., Sweet, J. R., & Ghosh, A. (2013). Evidence for tidal triggering of high-amplitude rapid tremor reversals and tremor streaks in northern Cascadia. *Geophysical Research Letters*, *40*, 4254–4259. https://doi.org/10.1002/grl.50832

Thomson, D. J. (1982). Spectrum estimation and harmonic analysis. *Proceedings of the IEEE*, *70*(9), 1055–1096. https://doi.org/10.1109/PROC.1982.12433

Tormann, T., Wiemer, S., & Mignan, A. (2014). Systematic survey of high-resolution b value imaging along Californian faults: Inference on asperities. *Journal of Geophysical Research: Solid Earth*, *119*, 2029–2054. https://doi.org/10.1002/2013JB010867

Tsang, L. L. H., Meltzner, A. J., Philibosian, B., Hill, E. M., Freymueller, J. T., & Sieh, K. (2015). A 15 year slow-slip event on the Sunda megathrust offshore Sumatra. *Geophysical Research Letters*, *42*, 6630–6638. https://doi.org/10.1002/2015GL064928

Uchide, T., & Ide, S. (2010). Scaling of earthquake rupture growth in the Parkfield area: Self-similar growth and suppression by the finite seismogenic layer. *Journal of Geophysical Research*, *115*, B11302. https://doi.org/10.1029/2009JB007122

Ueno, T., Maeda, T., Obara, K., Asano, Y., & Takeda, T. (2010). Migration of low-frequency tremors revealed from multiple-array analyses in western Shikoku, Japan. *Journal of Geophysical Research*, *115*, B00A26. https://doi.org/10.1029/2008JB006051

Utsu, T. (2002). Statistical features of seismicity, *International handbook of earthquake and engineering seismology, International Geophysics* (Vol. 81, pp. 719–732).

Wallace, L. M., & Beavan, J. (2010). Diverse slow slip behavior at the Hikurangi subduction margin, New Zealand. *Journal of Geophysical Research*, *115*, B12402. https://doi.org/10.1029/2010JB007717

Wallace, L. M., Beavan, J., Bannister, S., & Williams, C. (2012). Simultaneous long-term and short-term slow slip events at the Hikurangi subduction margin, New Zealand: Implications for processes that control slow slip event occurrence, duration, and migration. *Journal of Geophysical Research*, *117*, B11402. https://doi.org/10.1029/2012JB009489

Wang, K., Dragert, H., Kao, H., & Roeloffs, E. (2008). Characterizing an "uncharacteristic" ETS event in northern Cascadia. *Geophysical Research Letters*, *35*, L15303. https://doi.org/10.1029/2008GL034415

Watanabe, T., Hiramatsu, Y., & Obara, K. (2007). Scaling relationship between the duration and the amplitude of non-volcanic deep low-frequency tremors. *Geophysical Research Letters*, *34*, L07305. https://doi.org/10. 1029/2007GL029391

Wech, A. G., & Bartlow, N. M. (2014). Slip rate and tremor genesis in Cascadia. *Geophysical Research Letters*, *41*, 392–398. https://doi.org/10.1002/2013GL058607

Wech, A. G., & Creager, K. C. (2008). Automated detection and location of Cascadia tremor. *Geophysical Research Letters*, *35*, L20302. https://doi.org/10.1029/2008GL035458

Wech, A. G., Creager, K. C., Houston, H., & Vidale, J. E. (2010). An earthquake-like magnitude-frequency distribution of slow slip in northern Cascadia. *Geophysical Research Letters*, *37*, L22310. https://doi.org/10.1029/2010GL044881

Yabe, S., & Ide, S. (2014). Spatial distribution of seismic energy rate of tectonic tremors in subduction zones. *Journal of Geophysical Research: Solid Earth*, *119*, 8171–8185. https://doi.org/10.1002/2014JB011383

Yabe, S., & Ide, S. (2017). Slip-behavior transitions of a heterogeneous linear fault. *Journal of Geophysical Research: Solid Earth*, *122*, 387–410. https://doi.org/10.1002/2016JB013132

Yamada, T., Mori, J. J., Ide, S., Abercrombie, R. E., Kawakata, H., Nakatani, M., et al. (2007). Stress drops and radiated seismic energies of microearthquakes in a South African gold mine. *Journal of Geophysical Research*, *112*, B03305. https://doi.org/10.1029/2006JB004553

Zhang, J., Gerstoft, P., Shearer, P. M., Yao, H., Vidale, J. E., Houston, H., & Ghosh, A. (2011). Cascadia tremor spectra: Low corner frequencies and earthquake-like high-frequency falloff. *Geochemistry, Geophysics, Geosystems*, *12*, Q10007. https://doi.org/10.1029/2011GC003759